13

79570

UMI

MICROFILMED 1996

INFORMATION TO USERS

This manuscript has been reproduced from the microfilm master. UMI films the text directly from the original or copy submitted. Thus, some thesis and dissertation copies are in typewriter face, while others may be from any type of computer printer.

The quality of this reproduction is dependent upon the quality of the copy submitted. Broken or indistinct print, colored or poor quality illustrations and photographs, print bleedthrough, substandard margins, and improper alignment can adversely affect reproduction.

In the unlikely event that the author did not send UMI a complete manuscript and there are missing pages, these will be noted. Also, if unauthorized copyright material had to be removed, a note will indicate the deletion.

Oversize materials (e.g., maps, drawings, charts) are reproduced by sectioning the original, beginning at the upper left-hand corner and continuing from left to right in equal sections with small overlaps. Each original is also photographed in one exposure and is included in reduced form at the back of the book.

Photographs included in the original manuscript have been reproduced xerographically in this copy. Higher quality 6" x 9" black and white photographic prints are available for any photographs or illustrations appearing in this copy for an additional charge. Contact UMI directly to order.

UMI

A Bell & Howell Information Company
300 North Zeeb Road, Ann Arbor MI 48106-1346 USA
313/761-4700 800/521-0600

RICE UNIVERSITY

The Solar Wind Interaction with the Martian Ionosphere: Extension of the Venus Steady State Flow/Field Model

by

Dana M. Hurley

A THESIS SUBMITTED IN PARTIAL FULFILLMENT OF THE REQUIREMENTS FOR THE DEGREE

Master of Science

Approved, Thesis Committee:

Paul A. Cloutier, Chair
Professor of Space Physics and Astronomy

Richard A. Wolf
Professor of Space Physics and Astronomy

Tamara S. Ledley
Senior Faculty Fellow of Space Physics and Astronomy

Houston, Texas
May, 1996

UMI Number: 1379570

UMI Microform 1379570
Copyright 1996, by UMI Company. All rights reserved.

This microform edition is protected against unauthorized
copying under Title 17, United States Code.

UMI
300 North Zeeb Road
Ann Arbor, MI 48103

The Solar Wind Interaction with the Martian Ionosphere: Extension of the Venus Steady State Flow/Field Model

by

Dana M. Hurley

Abstract

A model is constructed to describe the magnetic field, the global current system, the electric field and the potential in the solar wind interaction with Mars assuming that Mars has no intrinsic magnetic field. It, therefore, incorporates the physics learned from the Pioneer Venus Orbiter, which observed the interaction of Venus, an unmagnetized planet, with the solar wind for 14 years. Integrating recent knowledge of the global current system at Venus [*Law* 1995] into the Flow/Field model of Cloutier *et al* [1987] and expanding the model to represent three dimensions, we adapt the Flow/Field model for application to Mars. We investigate the 3-D current system to learn the physics of the interaction. Then, the model is applied to test simple geometries in order to validate it. Future applications are discussed.

Contents

1. Introduction 1
   1.1 Pioneer Venus 2
   1.2 Probing Mars 4
   1.3 Motivation 6
2. Solar Wind Interactions 8
   2.1 The Solar Wind 8
   2.2 Solar Wind Interactions with Obstacles 10
   2.3 Solar Wind Interactions with Unmagnetized Conductors 13
2.3.1 Anatomy of the Interaction 13
2.3.2 Models of the Interaction 18
   2.4 Motivation and Method for Model Extension 21
3. Current Systems at Venus 24
   3.1 Currents Needed to Explain the Observed Magnetic Field 24
   3.2 Physical Processes for Driving Currents 29
4. The Model 33
5. Model Diagnostics 39
   5.1 Module Limitations 39
   5.2 Trial Cases 41
6. Conclusion 49
References 51

1. Introduction

Although Mars is Earth's next door neighbor, surprisingly little is known about how Mars interacts with the solar wind. In fact, it remains unknown whether Mars has an intrinsic magnetic field. During the past 30 years, we have sent space probes everywhere from the Sun to the far reaches of the solar system. But somehow, we have yet to get a magnetometer close enough to Mars to determine any more than an upper limit to its intrinsic magnetic field. The current best upper limit is a magnetic moment of a few times 10^{22} G•cm^3 [*Dolginov* 1978]. This low upper limit suggests that if Mars does have an intrinsic magnetic field, it is so small that it will by no means dominate the interaction of Mars with the solar wind. At most, it will contribute to a "hybrid" interaction with the conducting ionosphere.

The next hope towards gaining insight on the nature of the solar wind's interaction with Mars comes with the Mars Global Surveyor satellite. Although the primary objective of the spacecraft is to make a high resolution map of the surface, there is one plasma science instrument that is scheduled to be on board--a magnetometer. If the spacecraft is launched as scheduled in late 1996, data from the first orbits should begin streaming in around September 1997. This thesis develops a model which, when coupled with Mars Surveyor data, can be used as a diagnostic tool for the Martian interaction with the solar wind. It is based on the physics we have learned from in-depth investigations of Venus and on data from previous Mars missions.

To date, most of the research done on the solar wind interaction with unmagnetized but conducting objects, such as Venus, Mars and comets, has been focused on Venus. There is a significant amount of data on cometary interactions; however, comets lack the gravity necessary to retain their atmosphere as solar wind ion pick-up tries to accelerate the cometary ions and electrons down the tail. However, in the case of a planet-size obstacle, gravity is so strong that the loss of atmosphere due to ion

pick-up is negligible. Therefore data from comets is not usually used to study how Venus and Mars interact with the solar wind. Fortunately, there is a plethora of *in situ* data for Venus from the extremely successful Pioneer Venus mission.

1.1 Pioneer Venus

The Pioneer Venus Orbiter (PVO) was launched in 1978 and recorded data while in orbit around Venus for 14 years. PVO carried 17 experiments, 7 of which were used for plasma science: a solar wind plasma analyzer to measure properties of the solar wind; a magnetometer to characterize the magnetic field at Venus; an electric field detector to study the solar wind and its interactions; an electron temperature probe to study the thermal properties of the ionosphere; an ion mass spectrometer to characterize the ionospheric ion population; a neutral mass spectrometer to determine the composition of the upper atmosphere; and a charged particle retarding potential analyzer to study ionospheric particles.

The orbit of PVO was highly eccentric and carried it as close as approximately 150 km above the surface at periapsis. The orbit advanced such that periapsis slowly rotated to cover all solar zenith angles. For dayside periapsis orbits, often the spacecraft would pass across the bow shock and sample the upstream solar wind just prior to periapsis. On such a trajectory, PVO samples a large altitude range in a span of a couple of hours. A typical dayside periapsis orbit begins in the pre-shocked solar wind (altitude of ~1800 km), descends through the magnetosheath (400-1800 km) to the ionopause (occurring between 300-400 km), and finally reaches periapsis at some point in the ionosphere. Because the solar wind conditions can change on that time scale, one can not use the data from any one pass and its associated upstream parameters to draw conclusions about the effects of solar wind pressure on the ionosphere. Although it is impossible to know how the solar wind is changing during any one pass, one can assume that the solar wind conditions usually remain fairly constant. Then, one classifies large sets of data according to upstream solar wind conditions and

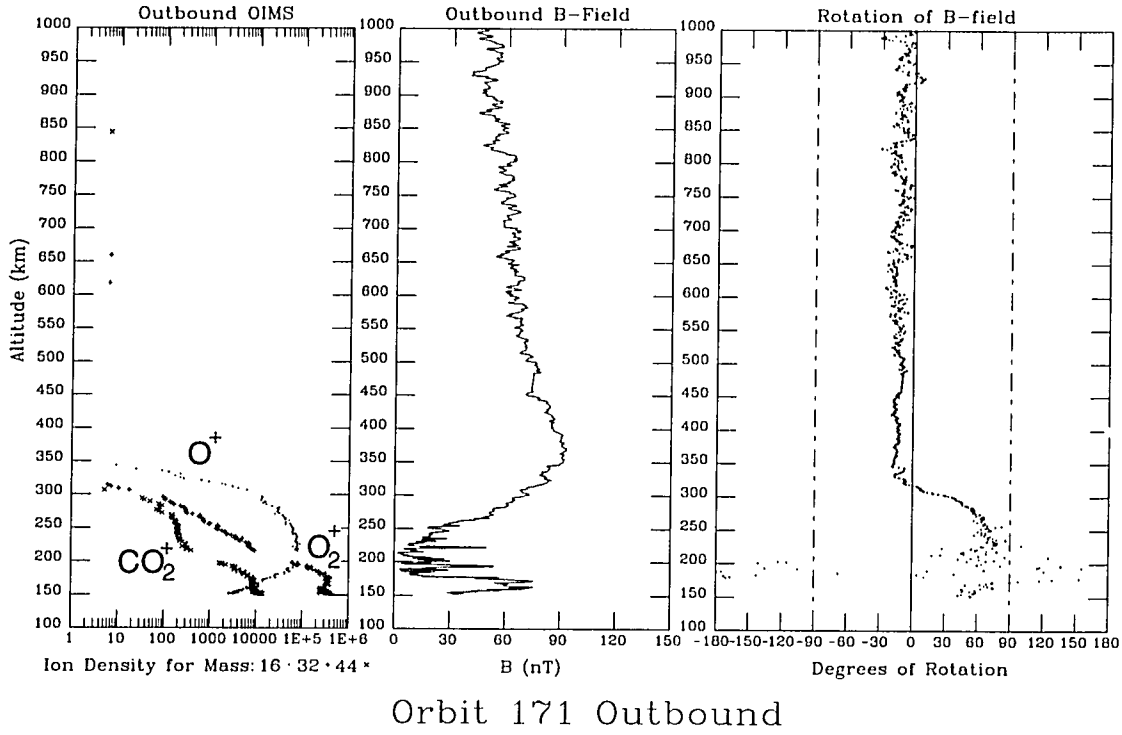

Figure 1.1--PVO outbound orbit 171. The left panel is the ion density as recorded by OIMS. The middle panel is the magnitude of the magnetic field from OMAG. The right panel is the direction of the magnetic field. All quantities are plotted verses altitude. The ionopause is from 290-350 km.

statistically analyzes the situation. Consequently, the anomalies average away.

Some of the most relevant PVO data come from the Orbiter Ion Mass Spectrometer (OIMS) and the Orbiter Magnetometer (OMAG). Comparing and contrasting these two data sets, we acquire details about the ionospheric composition and structure. For example, in figure 1.1 is the data from PVO outbound orbit 171. In the data, one can observe many features. First of all, the region encompassing the altitude in the ion data (left panel) at which the ions suddenly "turn-on" with a steep gradient in the dominant ion (O^+) concentration to the point where the slope of the ion density changes to the ionospheric scale height is the ionopause. In figure 1.1, this corresponds to altitudes of about 290-350 km. Turning to the OMAG data, we notice that at the same altitudes the magnetic field direction rotates 80° (right panel). The magnetic field strength

(center panel) also appears to begin decreasing at the same altitudes, but there is no correlation between magnetic field strength and ionopause location in statistical analysis of several orbits. However, *Law* [1995] demonstrates that the rotation of the magnetic field is a good indicator for the location of the ionopause.

Together, there is 14 years worth of data from Venus. Even four years after the end of the mission, not all of the data has been analyzed to its full potential. There are still many more interesting results to be found from the PVO archives.

1.2 Probing Mars

Unfortunately, a lack of appropriate magnetic field data from spacecraft which have probed Mars prohibits a decisive determination of what kind of obstacle the red planet presents to the solar wind. In the early 1970's, Mariner 4 and three Russian probes, MARS 2, 3 and 5, flew by the planet at distances far too great to penetrate the ionosphere [*Dolginov* 1978]. The magnetometer data from the missions establishes the location and shape of the bow shock. Researchers made many early speculations about the nature of the planetary magnetic field based on this data. However, without the benefit of the current understanding of the Venus interaction, many of the postulated ideas were merely conjecture.

Next, the two Viking landers descended to the surface of Mars. Although they were in the perfect position to measure the strength of Mars' intrinsic magnetic field, they were not equipped with magnetometers to do so. These missions were fruitful, though, in that they directly sampled the composition of the ionosphere and atmosphere as they landed. To detect the ion density, the Retarding Potential Analyzer (RPA) measured the current coming through a small opening. Knowing the instrument's retarding voltage and the spacecraft position and velocity, the current was processed to yield not only the ion composition and bulk velocity, but also the temperature and density of the components [*Hanson* 1977].

The two landers alit on the Martian surface at solar zenith angles of approximately 45°. Viking 1 landed during intermediate solar wind pressure and Viking 2 landed during high solar wind pressure, supplying data from two different states of the ionosphere. Studies of Venus indicate that the incident solar wind pressure greatly influences the structure of the ionosphere. We implement this information in the construction of a model atmosphere of Mars for use in this research.

More recently, PHOBOS 2 was dispatched to Mars. Its first four orbits were highly elliptical orbits, with a minimum periapsis altitude of 850 km. After the elliptical orbits, the spacecraft orbit circularized at an altitude of 6000 km for 80 passes before the spacecraft lost contact with Earth. Even the closest approach of 850 km kept the spacecraft too far away from the planet to determine more than an upper limit to the intrinsic magnetic field of Mars. The spacecraft did not penetrate the planetary ionosphere.

The established upper limit to the magnetic moment does suggest that if Mars does have an intrinsic field, it is very weak and plays only a small role in the interaction. In fact, studies of the limited data seem to indicate that Mars, like Venus, has an induced rather than intrinsic magnetotail [*Riedler* 1989]. PHOBOS 2 detected a change in the magnetic field polarity of the Martian tail lobe when Mars crossed an IMF sector boundary. This is a signature of an induced magnetotail, which is further explained in chapter 3. Although this is not conclusive, we will base the following model on the premise that Mars has no intrinsic magnetic field.

The latest mission to Mars, Mars Observer, had much potential for plasma science. The spacecraft was properly equipped to determine whether Mars has an intrinsic magnetic field. Unfortunately, Mars Observer lost contact with Earth during insertion into Martian orbit. Therefore, we must await results from future missions to discover the true magnitude of the Martian magnetic field, if one exists.

The best prospect for resolving this is the upcoming Mars Global Surveyor (MGS) mission. Although the primary objective of

the spacecraft is to make a high resolution map of the surface, the plasma science community will be represented by a magnetometer on board. Planned spacecraft launch in late 1996 would bring about insertion into Martian polar orbit in September 1997. If all goes well, we will be able to determine the nature of the interaction with only a few spacecraft passes. Despite the fact that there is only a magnetometer on board, we have found that much information can be deduced from the magnetic field data alone. In fact, we believe that with the model that is developed in this thesis, we can completely characterize the Martian interaction with the solar wind given only the magnetic field data from MGS orbits.

1.3 Motivation

This thesis is a testing ground for a model developed to characterize the physics of the solar wind interaction with unmagnetized, but conducting obstacles. We compile facets of the best models which describe the solar wind interaction with Venus to create a comprehensive three dimensional model of the interaction. Our goal is to extend the current best understanding of Venus to predict the manner in which the solar wind interacts with Mars.

In the past, many models have reproduced data from the Venusian ionosphere by solving the magnetohydrodynamic (MHD) equations for the set of boundary conditions specific to Venus. The Flow/Field model [*Cloutier* 1979, 1983, 1987] treats the problem two dimensionally and duplicates many features of the interaction in the PVO data with excellent agreement. However, *Law and Cloutier* [1995] discovered a rotation in the magnetic field direction at the onset of the Venusian ionopause which was not predicted by the 2-D model. Because the Flow/Field model neglects the current which produces the rotation, it is surprising that the Flow/Field model works as well as it does in other respects. To investigate the global current further, the model developed here incorporates the 3-D global current system into the physics of the Flow/Field model. Furthermore, this work breaks the global current system down into

separate physically meaningful current systems in a unique attempt to explain the physics driving the interaction.

In addition, this thesis is the first step towards applying the 3-D model to Mars. We extrapolate the conditions at Venus to Mars-like conditions and predict the form of the interaction at Mars. Using the extended model, we can predict the magnetic field everywhere in the ionosphere of Mars or just along an orbit of Mars Surveyor. If the model can correctly reproduce MGS data, we can be confident that Mars interacts with the solar wind, like Venus, as a conductor without a sufficient magnetic field. Also, we can be satisfied that we understand the physics of the solar wind's interaction with conducting obstacles.

Finally, it is important to glean as much information from the magnetometer on MGS as possible. In order to do so, we must understand the relationship between all the variables in the interaction. Therefore, we investigate the relationship between parameters in the solar wind interaction with Venus in order to extrapolate the results to Mars. Then, we can use the magnetic field data at Mars to compute several other quantities involved in its interaction. In fact, we find that the magnetic field data coupled with our model easily leads to the electric field, electric potential, and the global current. Once we establish these relations, we greatly increase the amount of information available from MGS and significantly improve the understanding of solar wind interactions with unmagnetized, conducting obstacles.

2. Solar Wind Interactions

2.1 The Solar Wind

The investigations into the existence of a solar wind were prompted by observations of comets and their tails in the early 1950's [*Biermann*]. As a comet approaches the Sun, its tail streams out behind it--always pointing away from the Sun. In contrast, as it continues past perihelion, the tail leads the comet away from the Sun. This observation called to mind the question--what makes the tail always point away from the Sun? Some kind of particle pressure in interplanetary space pushes the material away from the Sun. Other observations of a two component tail led to the discovery that a magnetic field accompanies the particle pressure. The cause of these features of a comet is a solar wind with an associated interplanetary magnetic field.

Later investigations into the nature of the solar wind revealed that it is a supersonic, superalfvenic magnetized flow of solar ions and electrons which are accelerated off the surface of the Sun and flow radially outward to the heliopause. Typical plasma densities, n_i and n_e, of the solar wind in the ecliptic plane at 1 AU are around 5 particles/cm^3. Its composition consists primarily of protons and electrons, although a few heavier nuclei are also found.

The solar wind streams with a highly varying radial velocity, v_{sw}, that almost always falls in the range of 300-1000 km/s. In fact, solar wind conditions are usually classified into three categories by the streaming velocity: low ($v_{sw} < 400$ km/s); medium ($400 < v_{sw} < 750$ km/s); and high speed ($v_{sw} > 750$ km/s). The solar wind varies on a time scale of hours, in general. Therefore, it is not unusual for conditions to change drastically between two consecutive spacecraft orbits. An interesting model which predicts solar wind speed by looking at solar magnetograms and solar helium images is developed by *Wang et al* [1989, 1996]. This model shows that the high speed winds seem to originate in coronal holes, regions in the solar corona where the magnetic field lines are open. Because coronal holes move from the poles towards the equator as the solar

cycle progresses from solar maximum to solar minimum, we can expect to see times of higher solar wind speed in the ecliptic plane during the declining phase of the solar cycle.

Using an average v_{sw} at 1 AU in the ecliptic plane of 400 km/s and typical ion temperatures, T_i, of 10^5 K, the solar wind near Earth has a Mach number, $\mathbf{M} = \mathbf{v}_{sw}/v_{sound}$, of approximately 8. Such a large Mach number allows us to assume the thermal gas pressure, $P_{gas} = nkT_i + nkT_e$, is negligible in the dynamics as compared to the plasma ram pressure, ρv_{sw}^2. Therefore, the approximate total pressure, energy and momentum of the solar wind are due to its ram pressure.

In addition, the solar wind magnetic field can be considered to be "frozen" to the particles. Therefore, as the solar wind plasma

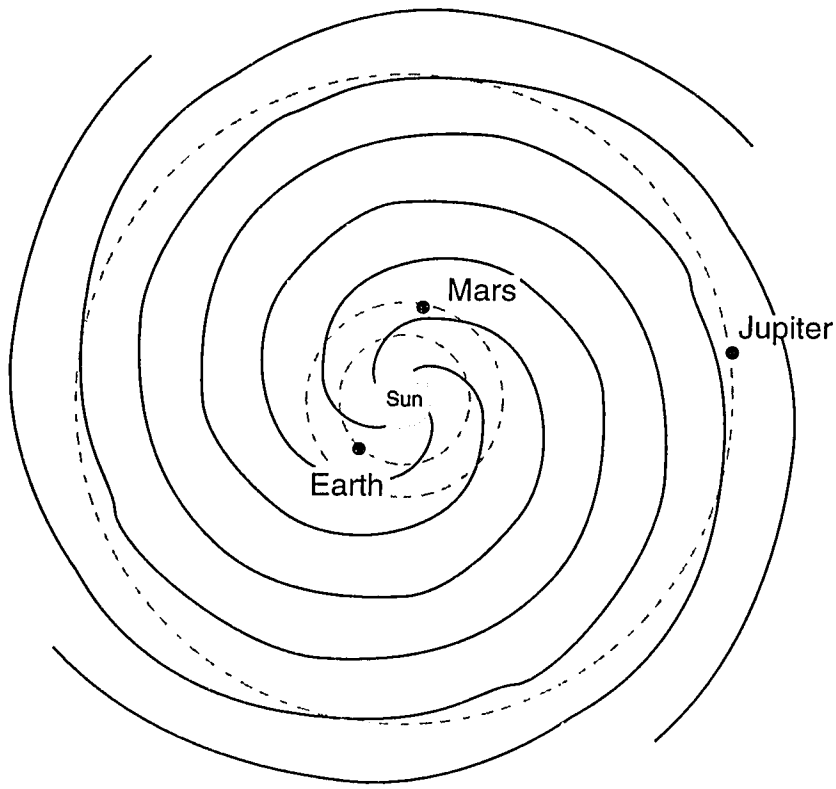

Figure 2.1--The Parker Spiral. As the magnetic field lines of the solar wind are tied to the plasma, they trace the path of a charged particle leaving the solar corona with an initial rotation velocity of the solar rotation speed. The radial velocity of the particle is constant; so spiral spokes are equidistant apart.

For reference, the approximate locations of the orbits of the Earth, Mars and Jupiter are shown. Note, the Sun and planets are not drawn to scale.

flows through the heliosphere, it carries along the solar magnetic field, forming the Interplanetary Magnetic Field (IMF) (see figure 2.1). The IMF lines trace out a spiral pattern called the Parker spiral. The IMF strength is typically around 5 γ (or 5 nT). The direction of the field is given nominally by the Parker Spiral or "garden hose angle." From figure 2.1 one can see that at Earth the angle between the IMF and the Earth/Sun line is about 45° on average.

However, like the solar wind speed, the IMF direction is highly variable. First of all, the angle between the magnetic field and the Earth/Sun line can vary by many tens of degrees. Second, spacecraft observe almost instant polarity reversals in the solar wind. This much larger effect--a change of the sign of B_r--is due to sector boundary crossings. Because the ecliptic plane is not aligned with the magnetic equator of the Sun, the ecliptic plane samples magnetic field alternately from the solar northern and southern hemispheres. The solar magnetic field is roughly a dipole field. Therefore, one hemisphere is dominated by outward pointing field lines while the other holds the inward ones. Likewise, a planet orbiting the Sun in the ecliptic plane experiences alternating periods of IMF polarity.

2.2 Solar Wind Interactions with Obstacles

As the solar wind flows supersonically through the solar system, it occasionally must flow past an obstacle (*e.g.*, a planet). When the solar wind encounters an obstacle, it must be slowed to subsonic speeds, then be diverted around the obstacle in order to remain in steady state. In the solar system, we observe three different types of obstacles to the solar wind, each having its own signature interaction.

First of all, for objects with an intrinsic magnetic field, such as the Earth, Mercury and the outer giant planets, magnetic pressure from the planetary magnetic field is sufficient to stand off the solar wind at some distance above the surface of the planet (see figure 2.2A). A bow shock forms upstream of the planet to slow,

heat and compress the solar wind plasma. Inside the shock boundary, the shocked plasma proceeds at subsonic speeds and is forced to flow around the planetary magnetosphere. At the point where the magnetic pressure of the planetary magnetic field equals the total pressure of the shocked solar wind ($B^2/2\mu_o = \rho v^2$), we have the magnetopause. In a zeroth order approximation, the solar wind plasma does not penetrate the magnetopause boundary. Therefore, in effect, the magnetopause demarcates the separation of the solar wind plasma from planetary plasma.

As the solar wind pressure changes, the location of the magnetopause moves back and forth, compressing the planetary magnetic field enough so that the magnetic pressure just balances the solar wind pressure. As the impinging solar wind compresses the field, it puts a force on the planetary core. Through this, the solar wind momentum is transferred to the planet.

One important signature of this brand of solar wind interaction is the planetary magnetotail. For reasons beyond the scope of this thesis, the intrinsic dipole magnetic field of the planet is compressed on the dayside and stretched into a long tail on the nightside. The tail consists of two lobes of opposite polarity separated by a current sheet. Because the field in the magnetotail is composed of planetary magnetic field lines, the direction of the field in the lobes is dictated by the direction of the planetary dipole. In addition, the polarity of the tail lobes will not change unless the dipole field itself reverses polarity.

In contrast, for objects without precursors, like an intrinsic magnetic field (*e.g.*, the Moon), nothing exists to modify the surroundings and forewarn the solar wind of the obstacle's presence. Therefore, as is shown in figure 2.2B, the solar wind particles simply collide with the surface of the obstacle. Upon impact, the ions and electrons neutralize. Because they strike the planet with momentum $\rho \mathbf{v}_{sw}$, they transfer their momentum directly to the object. Behind the planet, there is a region which is void of solar wind particles, as all the ones that would have been there are

A. SOLAR WIND INTERACTION WITH THE EARTH

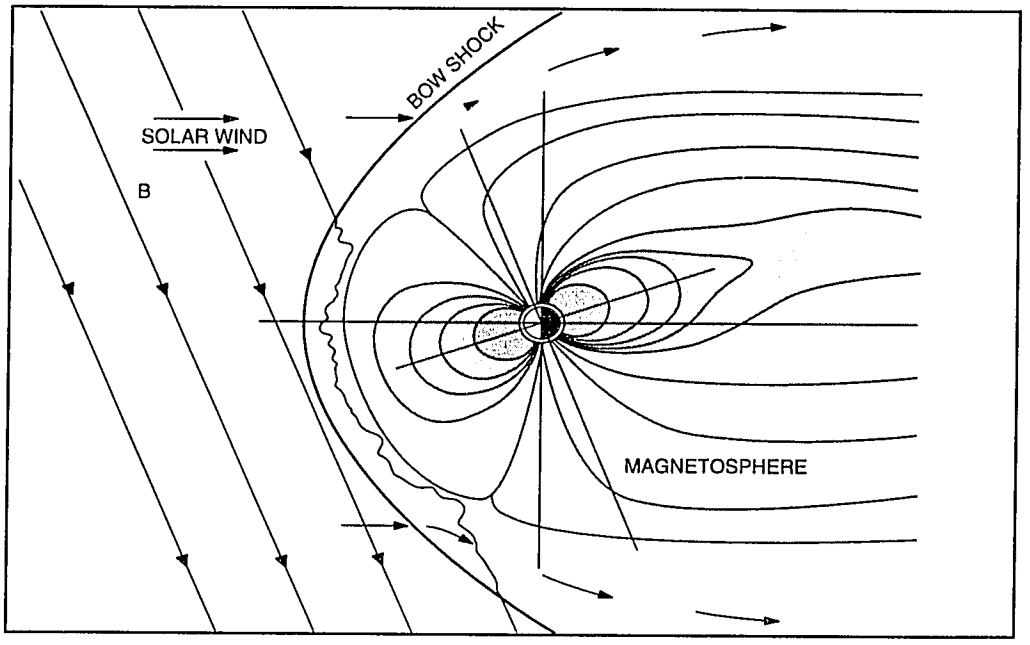

B. SOLAR WIND INTERACTION WITH THE MOON

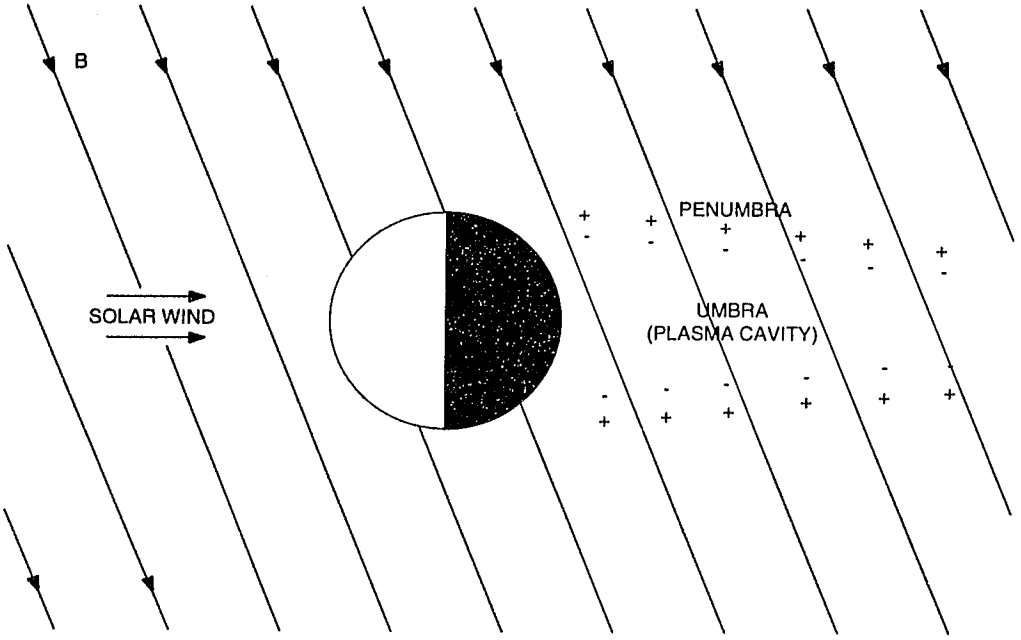

Figure 2.2--A. The solar wind interaction with an obstacle with a substantial intrinsic magnetic field. The solar wind compresses the magnetic field on the dayside of the obstacle. The tail lobe stretches far behind the planet.

B. The solar wind interaction with the moon. The solar wind particles are not deflected around the moon. Therefore, there is a cavity without solar wind particles behind the planet and a rarefaction wave as the particles begin to fill the region in. Because there is no electromagnetic interaction, the magnetic field is constant. *(Courtesy of C. Law)*

blocked by the planet. That region fills in as the thermal velocity of the nearby particles carries them into the region.

The third type of interaction is one in which the obstacle is unmagnetized, yet is sufficiently conducting to sustain electric currents. This situation occurs in comets and planets with a substantial atmosphere, but no intrinsic magnetic fields. For instance, Venus has a substantial dayside ionosphere, but no intrinsic magnetic field. The impinging solar wind drives currents in the ionosphere and magnetosheath of the planet which modify the local IMF. Together, the IMF and the field from the induced currents produce a draping of the magnetic field around the planet (see figure 2.3). This current system is broken into components and discussed in depth in chapter 3.

Because the solar wind must be diverted around the planet, a bow shock forms upstream of the planet to slow and heat the plasma. The shocked solar wind plasma flows freely along the draped field lines. This configuration serves to deflect most of the solar wind flow around the unmagnetized, conducting obstacle. However, a small percentage of the field lines actually penetrates the obstacle and interacts directly with the planetary ionosphere. This small percentage of penetration drives many processes in the ionosphere which cascade down to transfer the incoming solar wind momentum to the planetary surface. It is the details of this brand of solar wind/obstacle interaction that this thesis will consider.

2.3 Solar Wind Interactions with Unmagnetized Conductors

2.3.1 Anatomy of the Interaction

In order to understand the interaction of the solar wind with an unmagnetized conductor, follow the time evolution of one magnetic field line in the solar wind flow as it approaches Venus. Nine time steps are depicted in figure 2.3. As the solar wind approaches the bow shock, it sees no precursor to the obstacle; therefore, at line #1 in figure 2.3, the plasma retains the conditions of the ambient solar wind. The charged particles stream radially at about 400 km/s. The solar wind flow is magnetized, but the field is

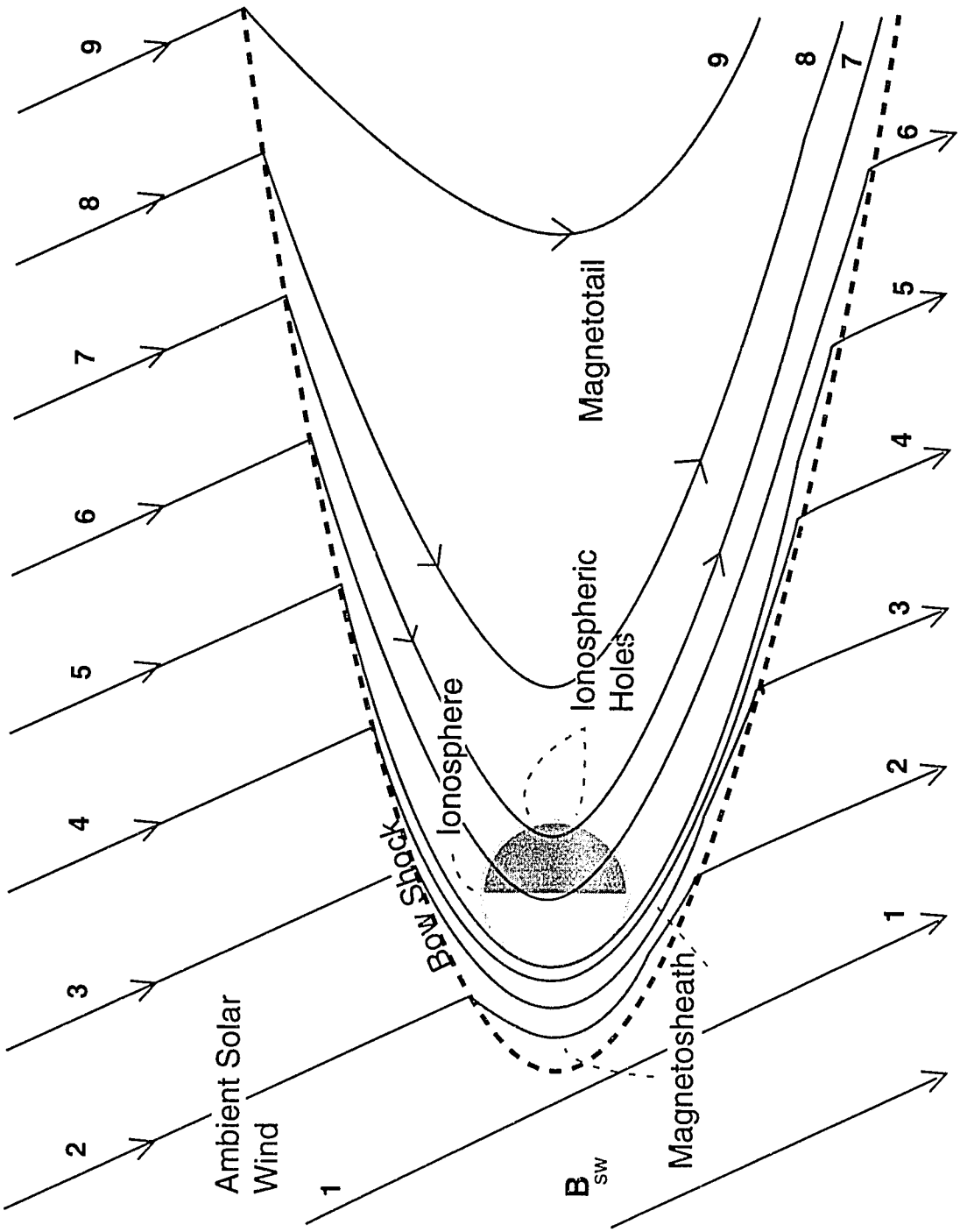

Figure 2.3--The solar wind interaction with Venus. Each field line represents the next step in a time progression, with field line 1 being the earliest time. The Sun is to the left in this diagram and the solar wind flow direction is to the right. Each line is described in the text of section 2.3.1.

"frozen-in." Locally, the IMF field lines simply move along in straight lines with the plasma. The upstream problem can be treated as a steady state.

The plasma conditions are modified, however, when the field line encounters the bow shock. The bow shock serves as the primary warning to the solar wind that there is an obstacle ahead. It is located about 1.3 R_V in front of Venus (and less than 1.6 R_m from Mars). At the bow shock, the plasma is heated and slowed to a subsonic speed. Applying the familiar Rankine-Hugonoit shock/jump relations to the upstream solar wind conditions yields the values immediately after the shock for plasma velocity. density, pressure, temperature, and magnetic field strength.

Proceeding to the post-shock region called the magnetosheath (the light gray region in figure 2.3), the flow is still best handled with the gasdynamic equations. Therefore, the post-shock values for velocity, density, etc., can be propagated downstream to all other positions in the magnetosheath from the post-shock values using the gasdynamic relations along streamlines. Using the gasdynamic relations, one finds the plasma velocity along the planet-Sun line decreases to zero at the front of the obstacle. This point is named the sub-flow point and the velocity is purely tangential to the obstacle there.

Because the bow shock is curved, the incoming field lines will first meet the shock at a single point. Then as the field line progresses downstream at the solar wind speed, a greater percentage of the field line will be inside the magnetosheath. For example, field line 3, one time step later than field line 2, is more immersed in the magnetosheath than line 2. However, because the portion of the field line inside the bow shock moves much slower than its unshocked part, the field lines bend at the bow shock. In addition, the part that first enters the bow shock moves slower than the rest of its line for the longest period of time. Therefore, it lags much further behind than the parts that entered the magnetosheath at later times. The resulting field lines exhibit increasing

curvature, as lines 2, 3, 4, and 5 demonstrate, with each time step in figure 2.3.

If the planet is an impenetrable object, the solar wind velocity must be purely tangential along the boundary to the solar wind. In that case, there is no mixing of the solar wind plasma with the planetary plasma. Thus, the ram velocity of the particles that travel along the planet/Sun line decreases steadily until it slows to zero at the sub-flow point. Because the plasma is not moving inwards at the boundary and the magnetic field is tied to the plasma, the magnetic field is also stationary at that point. Therefore, in ideal situations, the innermost field line stagnates on the sub-flow point, like line 5 in figure 2.3. When several field lines are considered, there is a net build up of magnetic flux in front of the planet as the particles are diverted around the planet. This effect is called the "draping" of the magnetic field around the planet. Interestingly, one can see in figure 2.3 that regardless of the "garden hose angle" with which the field line approaches the planet, the magnetic field lines are almost locally horizontal when they are near the planet. This fact will simplify the calculations in the model.

In reality, the field lines do not actually stop at the stagnation point. Eventually, as with field line 6, the field line goes around the planet, traveling through the ionosphere of the obstacle to the nightside. However, as the field line reaches the ionopause, solar wind ion pick up mechanisms cause mass loading of the field line by cold planetary ions. As the solar wind attempts to strip the planet of some of its ions, a piece of the field line penetrates the ionosphere. Ionospheric particles are moving much slower than those in the magnetosheath, so the portion embedded in the ionosphere is "grabbed" by the slow particles. Meanwhile, the outside portion attempts to pass the planet. In doing so, the next segment of the field line comes in contact with the ionosphere and even more of the field line gets trapped. The geometry (see figure 2.4) is such that inside the ionosphere, the magnetic field rotates to point directly to or away from the sub-flow point. However, at the topside of the ionopause, the field bends back to its draped

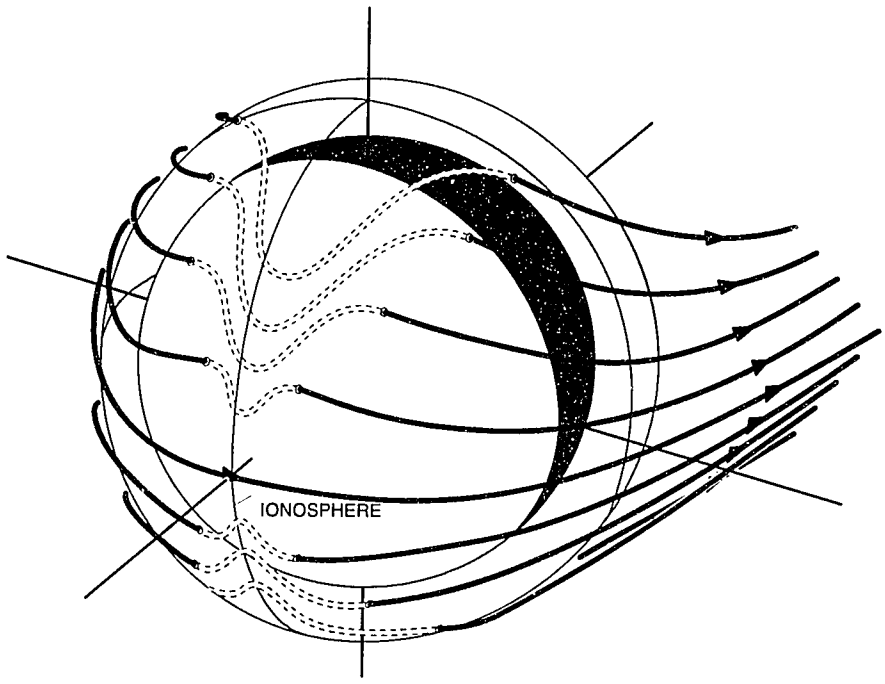

Figure 2.4--The form of field lines in the ionosphere. As the magnetic field lines enter the ionosphere, they suffer drag due to mass loading. The net effect is that the field lines form a "weathervane" pattern on the dayside of the planet. *(Courtesy of C. Law)*

configuration at the ionopause. This effect is observed in PVO magnetometer data as a rotation in the direction of the magnetic field at the ionopause [*Law* 1995].

Inspecting the region behind the planet in figure 2.3, the draped field lines stretch to extend very far down the tail. These field lines (# 6, 7, 8, and 9) compose the induced magnetotail of the planet. Because the IMF direction points toward the bottom of the figure, the magnetic field in the top half of the tail lobe will be directed mostly to the left while the field in the bottom lobe points right. Because the tail comprises the solar wind magnetic field, the polarity of the tail lobes is dependent on the polarity of the IMF. Therefore, when a sector boundary is crossed and the direction of the IMF direction is reversed, the tail lobe polarity should also switch. This is an important signature of an unmagnetized conductor's interaction with the solar wind. *Riedler* [1989] reported a reversal in tail lobe polarity at Mars during the PHOBOS 2 mission

when the planet crossed an IMF sector boundary. If Mars has an intrinsic magnetic field, the planetary dipole field would have had to have flipped in order to explain that observation. Because it would be a tremendous coincidence that a spacecraft would happen to be there for such a rare occurrence, this observation leads us to believe that Mars does not have a magnetic field of its own.

By the time the middle of the field line reaches the nightside of the planet (line 7 in figure 2.3), the ends of the line, which have been traveling at the solar wind speed, extend very far downstream. The geometry requires that the field line points radially outward from the planet at the two places the field line loses contact with the ionosphere. With a small portion of the field line still attached to the back of the planet, there is an easy path for solar wind ions to travel directly down the field line into the ionosphere. PVO has detected a dramatically reduced ion density at certain positions on the nightside of Venus which correspond to the place where the field lines turn radially out into the magnetosheath [*Marubashi* 1985]. For that reason, these places have been named ionospheric holes. Once the field line detaches from the planet, as in lines 8 and 9, magnetic tension starts to pull the middle of the field line back towards the ends. Eventually, far downstream from the obstacle, the IMF returns to its original configuration.

2.3.2 Models of the Interaction

The Spreiter and Stahara Model

Spreiter and Stahara [1980] and *Spreiter et al* [1970] have developed a model which reproduces the magnetosheath very well on the dayside of the terminator. Their model is a purely gasdynamic treatment of a supersonic wind hitting an impenetrable hemisphere attached to an infinite cylinder. Assuming frozen-in-flux, they treat the magnetic field as an afterthought. The model's only input parameter of H/r_o (the atmospheric scale height divided by the obstacle size) can be altered to adapt the model to the dayside of any planet. Using an H/r_o of .10 for Venus, their results accurately determine the position and the shape of the bow shock. Additionally,

their values for velocity, density, temperature and pressure reproduce observed data excellently.

One important limitation of the Spreiter and Stahara model is that it is only valid on the dayside magnetosheath. Because they use an infinite cylinder as the obstacle shape past the terminator, the geometry ceases to resemble the physical problem. Moreover, their boundary conditions simulate an impenetrable boundary at the planet. This gives excellent magnetosheath values, but it completely neglects our region of interest--the ionosphere. Therefore, an additional model must be used to describe the small amount of solar wind plasma that reaches the planetary ionosphere. The Flow/Field model is such a model.

The Flow/Field Model

In reality, a small amount of the solar wind permeates the ionosphere and must be considered in the interaction between the impinging flow and the planetary particles. In a series of papers [*Cloutier* 1979, 1983, 1987], *Cloutier et al* have developed a steady state magnetohydrodynamic (MHD) model to treat the ionosphere in the solar wind interaction with Venus--the Flow/Field model. It treats the ionospheric absorption of a few field lines as being equivalent to the ionosphere having a finite, but large, electrical conductivity. The two dimensional model solves the time-independent equations of MHD in the ionosphere with specified boundary conditions. Model results accurately reproduce many features of ionospheric structure observed in the PVO data, so we are confident that the model includes the dominant physics of the interaction.

The Flow/Field model takes the MHD equations and makes the following simplifying assumptions. First of all, in an ionosphere of several ion species, it assumes overall charge neutrality and single ionization. Therefore, the number density of ions equals that of the electrons, $n_i = n_e$. Second, because conditions are generally much more uniform in the local horizontal direction than the vertical direction, it approximates that the horizontal gradients are

negligible as compared to the vertical gradients. Therefore, only the vertical gradients contribute in the MHD equations. Moreover, simplifying assumptions reduce the electric field and current density. The Flow/Field model presupposes that the vertical current density is insignificant compared to horizontal currents. Also, the electric field is assigned to be constant and horizontal, directed perpendicular to the magnetic field with a magnitude of $E_y = -v_z B_x$, where E is the electric field, v is the flow velocity, and B is the magnetic field. Throughout the model, the **z** direction is the local vertical and **x** designates the direction aligned with the horizontal magnetic field. Finally, solving the simplified MHD differentials in the ionosphere, the Flow/Field model accurately reproduces PVO data.

One surprising result of the Flow/Field model simulations is that it produces the ionospheric magnetic field magnitude profile using only a two dimensional analysis. The discovery of a current system in the ignored dimension of the Flow/Field model called in to question whether the Flow/Field model accurately described the physics of the interaction. One would expect the magnetic field profile to be modified somewhat with the addition of currents in a third dimension. However, further research by *Law* [1995] explains that the currents neglected in the 2D model run along magnetic field lines. Thus, they rotate the direction of the magnetic field, but do not contribute to the magnitude. In this way, the two dimensional model is accurate for the magnitude of the magnetic field, but gives no information of the direction.

In looking at the pressure components in the ionosphere due to flow pressure, gas pressure, magnetic pressure and gravity, it appears that the sum of pressures does not total to the incident solar wind ram pressure. Because pressure balance throughout the entire region is required, there must be an element of pressure not accounted for in the model. Although PVO was not equipped to measure such high energy particles, it detected a possible population of superthermal ions at high altitudes which were not

included in the calculations [*Kramer* 1993]. These are candidates for the source of the "missing pressure."

In 1991, *Stewart* extended this model for application to Mars. In his model, he not only converts atmospheric conditions and scales to apply to Mars, but also amends the program to calculate the amount of pressure that was not included in the magnetic, gas, gravitational, and ram pressure terms that was still needed to total the incident solar wind pressure. Then, by including the "missing pressure" in the energy and momentum equations, he found that the Flow/Field's external heat input was unnecessary. Apparently, the unidentified pressure element supplies the heat necessary to complete the energy transfer and to reproduce the ion concentration profiles measured by the two Viking landers.

To date the Flow/Field model works well, but it needs to be updated. Specifically, we want to extend the Flow/Field model to treat the problem in three dimensions. That entails broadening the local view of the Flow/Field model into a comprehensive global picture satisfying global boundary conditions. Additionally, we modify the model to focus on the determination of other quantities. Using the former model, we have already developed a good understanding of the relationships between the magnetic field, ion densities, pressure, and energy. However, we apply what we know about these quantities to calculate other parameters, such as the electric field and electric potential. In the upcoming chapters, we present a method of incorporating these ideas in the Flow/Field model.

2.4 Motivation and Method for Model Extension

In order to completely describe the problem, we need to perform a full 3-D calculation. This thesis takes the initial steps by expanding the 2-D Flow/Field model into 3-D. The motivation behind this extension is that there are several aspects of the interaction which can only be accurately represented in three dimensions. These aspects include:

- characterizing the interaction globally

- implementing global boundary conditions
- incorporating the 3-D current system discovered by *Law and Cloutier* [1995]
- analyzing the physics of the parallel and perpendicular currents
- extrapolating the model to Mars
- calculating new parameters, such as the electric field and potential
- connecting the model to MGS data.

In doing so, we generalize the model to describe the physics of the interaction of a conductor in the solar wind on a global level. This is an improvement on the Flow/Field model which treats the problem locally.

In order to accomplish the full 3-D calculation, we take several steps:

- include a global magnetic field derived from observations
- integrate the global current system into the model
- investigate the physics of the global current system
- create model atmospheres for Mars and Venus
- calculate the electric field and electric potential self-consistently
- compare features of the interactions of Mars and Venus
- predict the magnetometer data for MGS orbits.

In this thesis, we develop and validate the modules to perform the first 5 steps on the list, including self-consistency checks for each calculation. The global magnetic field and current system to be used in steps 1 and 2 are from *Law and Cloutier* [1995]. Similarly, we discuss in detail the investigation of the physics of the global current system. This is accomplished by breaking the current into subsystems, as discussed in chapter 3.

The next steps (6 and 7 on the list) include doing the actual calculations with the real data. This is left for future work. Once we make the calculations with real data, we can follow two

interesting routes. One is to vary parameters on both the Mars and Venus models and investigate the effects these parameters have on the interaction. Another is to predict the form of the ionospheric interaction of Mars. When MGS reaches Mars, we can compare the real data with our predictions. Therefore, there are many exciting results to come from extending the Flow/Field model into 3-D. It is only in this way that we can truly understand the driving mechanisms of the solar wind interaction with an unmagnetized, conducting obstacle.

3. Current Systems at Venus

The overall configuration of the electric current density at Venus can be determined by superposing the different current systems necessary to produce all of the observed magnetic field features. Conversely, the required current density can be analyzed by dividing the total current into components driven by physically meaningful sources. Once we interpret these components, we learn the physics of how ionospheric currents flow. Then, if we are given only magnetic field data from a planet, we can break the field into parts and deduce many other important parameters based on the required currents.

3.1 Currents Needed to Explain the Observed Magnetic Field

In order to find the total current needed in the Venus/solar wind interaction, we take another approach to envision the draping of solar wind magnetic field lines around the planet. First, we study the draping by looking at electromagnetic effects of imposing an external magnetic field on a conductor. In general, a conductor always attempts to conserve the amount of magnetic flux threading it. Therefore, when an external magnetic field is imposed on a conductor, the change in flux induces an electric potential in the conductor. The potential causes electric currents to flow which produce their own magnetic field in the direction to oppose the external magnetic field. This field modifies the magnetic field in the vicinity of the conductor. For an infinite conductor, it can always exactly cancel the external field inside the conductor.

The resulting magnetic field from the cumulative effects of the IMF and the conductor's induced field is a magnetic field that appears to be draped around the planet. In the particular case of Venus, the dayside ionosphere of Venus is a relatively good conductor. Additionally, there is no insulator present to prohibit currents from flowing freely from the planetary ionosphere to the solar wind. Therefore, the IMF induces currents to run between the solar wind and the ionosphere. These currents produce the axial

magnetic field that, when added to the IMF, cancels the magnetic field interior to the ionosphere and creates the draped magnetic field pattern around Venus. The ionosphere/magnetosheath current pattern that produces the draping can be expressed as three separate currents--an open system in the magnetosheath and two closed systems in the ionosphere.

First of all, there is the "open" current system that flows along the bow shock and connects to the planetary ionosphere (see figure 3.1). Notice that the IMF does not deviate from the ambient conditions outside the bow shock. Therefore, the currents flowing along the bow shock must have a closure current somewhere within the interaction region. The actual form of the current is a solenoid-like configuration of nested current loops that only affect the magnetic field interior to them. However, the model developed here does not include most of the magnetosheath or the portions of the current loops located there. Therefore, as far as the model is concerned, this current is not divergence-free:

$$\nabla \bullet \mathbf{j} \neq 0$$

where **j** is the vector electric current density. Hence, this system is called an open current system.

As the open current flows along the bow shock, it produces many effects. One effect of the open current is an increased magnitude of the field from the IMF value. Looking at the currents face on, they appear as nested current loops. The point in the center of the loops is surrounded by more current than the points further out, and therefore, suffers the largest change in magnetic field strength. In addition, a current parallel to the magnetic field rotates the IMF to produce the field line curvature observed in the magnetosheath. Therefore, as the open current flows along the bow shock it bends the IMF field lines as they cross the boundary and increases the field strength in the magnetosheath.

After the open current flows along the bow shock, it shorts across to the ionosphere, returns along the dayside of the planet, and finally jumps back to the bow shock (see figure 3.1). The exact path

of the current through the dayside ionosphere is a function of the ionospheric conductivity. Although the current wants to flow on the path of least resistance, sometimes it is advantageous to travel a

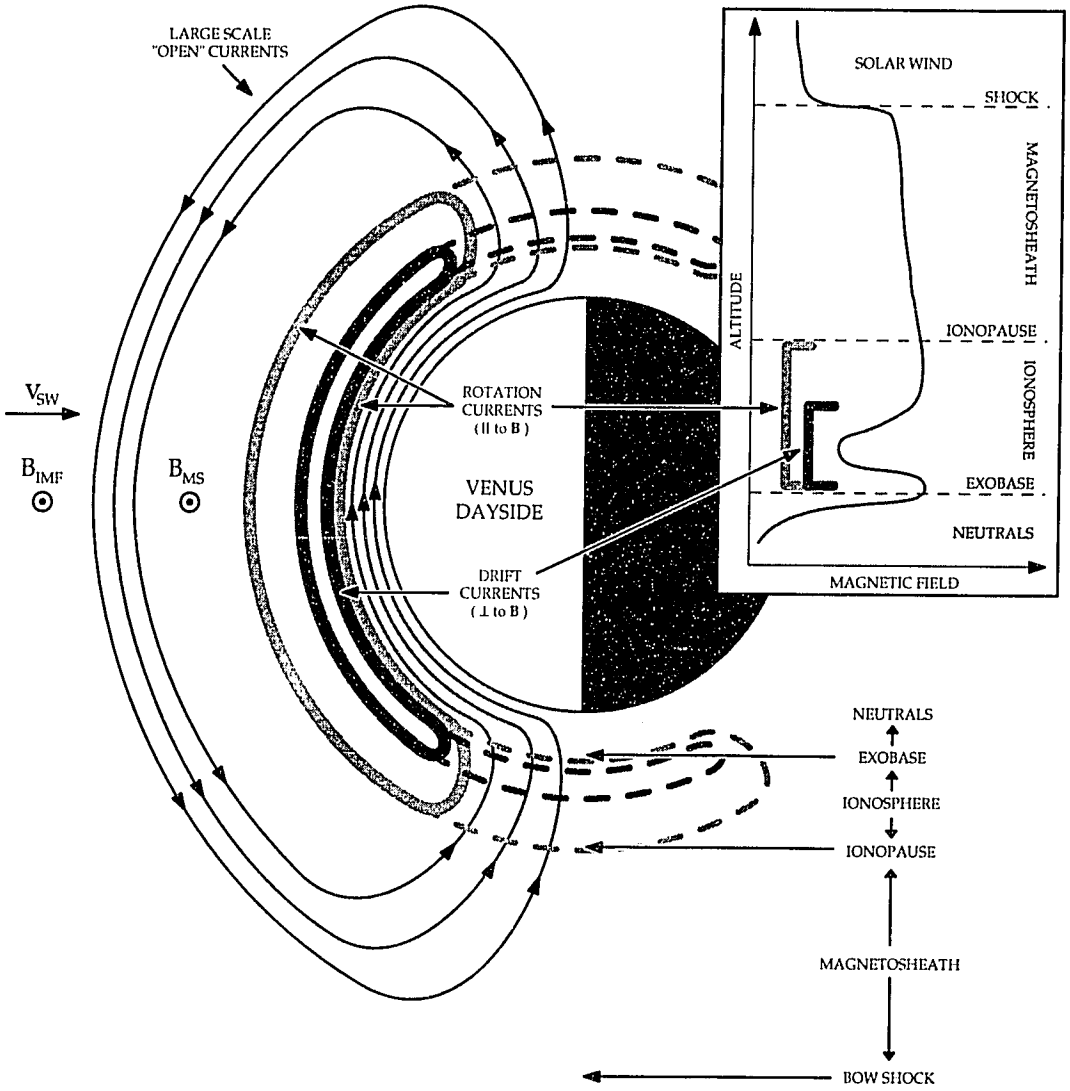

Figure 3.1--A picture of the global current system. There are three separate currents depicted. The large scale "open" current runs along the bow shock and connects to the ionosphere. A "closed" current parallel to the magnetic field at the ionopause causes the rotation of the field observed in PVO data. Also, a "closed" perpendicular current in the ionosphere produces the observed magnetic field magnitude profile, such as the one in the inset. Both these currents are "closed" systems, in that the entire current system is contained in the model. The figure depicts the location of the "closed" current systems, but not the direction. *(Courtesy of C. Law)*

shorter distance through a higher resistance. Therefore, the actual path of the ionospheric current can be calculated by minimizing the Joule heating:

$$\delta \int \mathbf{j} \bullet \mathbf{E} = 0$$

where **E** represents the electric field vector.

As a consequence of the ionosphere having a finite conductivity, some of the external magnetic field penetrates the ionosphere. The external field induces currents that oppose the field, but can not completely cancel it inside the conductor. Thus, the residual IMF embeds itself in the ionosphere and contributes to the dynamics of that region. Observations indicate that the magnitude of the ionospheric magnetic field has an altitude profile like that shown in the inset of figure 3.1. Due to Ampere's law:

$$\nabla \times \mathbf{B} = \mu_o \mathbf{j}$$

where **B** is the magnetic field vector and μ_o is the permeability of free space, it is apparent that any current perpendicular to the magnetic field evokes a change in its magnitude, while a parallel current alters its direction. Therefore, the magnitude changes in the altitude profile must be caused by currents perpendicular to the magnetic field. They are represented by the dark gray current in figure 3.1. However, observations also note a rotation of the magnetic field at the ionopause. From Ampere's law, the rotation region requires an associated parallel current (the light gray current in the figure). Both of these currents exist entirely within the ionosphere. They are divergence free within the framework of the model. Therefore, they are called "closed" current systems.

The exact ionospheric magnetic field pattern requires an almost pie-like ionospheric current configuration for its production. *Law* [1995] calculates the global current depicted in figure 3.2 based on a global ionospheric magnetic field constructed from PVO data. A parallel current in the rotation region aligns the magnetic field with the anti-sunward direction of the plasma motion. At lower altitudes, the perpendicular current creates the observed magnetic

A. Wire Segment View

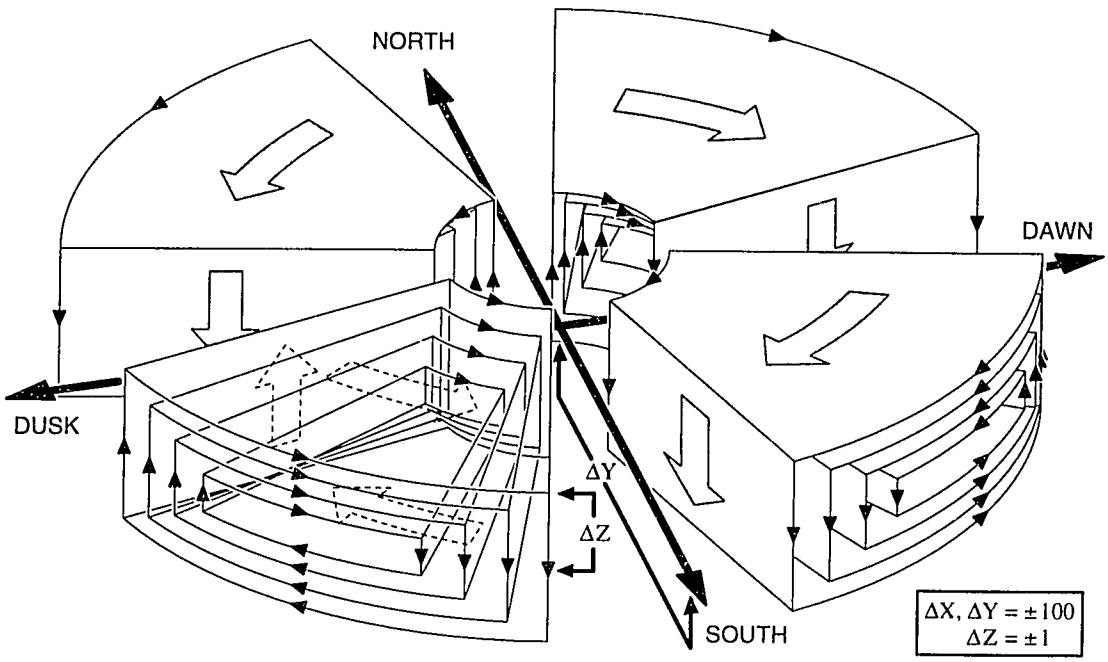

B. 3-D Global View

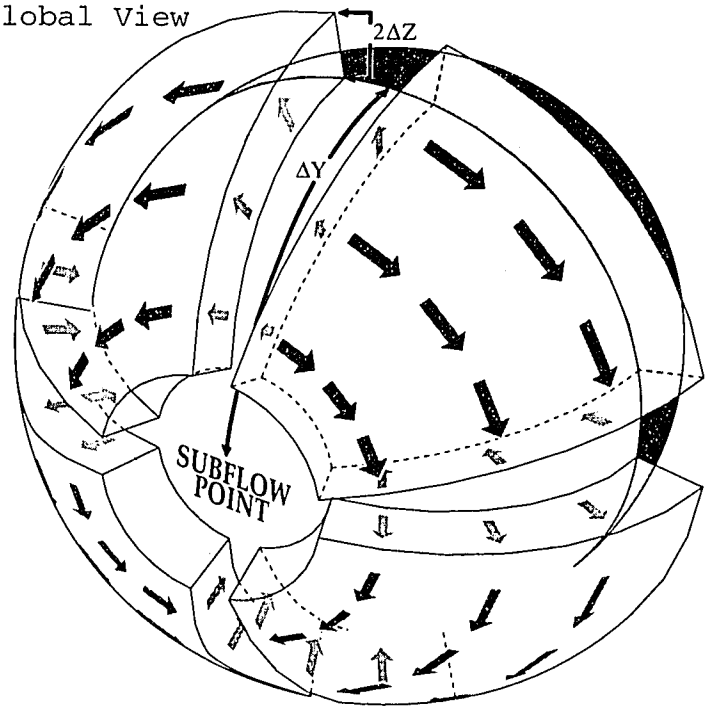

Figure 3.2--Form of the global 3-D current needed in the ionosphere to produce the global 3-D magnetic field observed by PVO. The symmetry of the problem shows that the current is similar in each quarter of the dayside of Venus. *(Courtesy of C. Law)*

field magnitude profile that was explained by the 2-D Flow/Field model. Finally, the closure current appears at the bottom of the ionosphere.

3.2 Physical Processes for Driving Currents

Once the configuration of the currents is established, we interpret the processes that drive these currents. This reveals the physics that governs the interaction between the solar wind and a Venus-like obstacle. We decompose the global current into major components, which include the direct current, collisionally driven currents, and drift currents.

Ohm's law states that an electric field induces a current to flow. The magnitude and direction of the current are equal to the dot product of the conductivity of the medium and the electric field:

$$\mathbf{j} = \sigma \bullet \mathbf{E}$$

where σ is the conductivity. Due to the presence of a magnetic field in the ionosphere, the conductivity is anisotropic and must be represented in tensor form. There is the direct conductivity, σ_0, which expresses how easily currents flow along magnetic field lines, and the Cowling conductivity, σ_3, which relates the ability to conduct currents across field lines. Therefore, the direct current, which is parallel to the magnetic field line, simplifies to $\sigma_0 E_{//}$. The perpendicular current, however, can be divided further.

The Cowling conductivity comprises two collisionally based currents, the Pederson and Hall currents. Although the ions and electrons **ExB** drift in the same direction, they encounter a different number of collisions. The collision frequency for the ions is dependent on one atmospheric parameter, the particle density, while the electron collision frequency also incorporates an electron temperature dependence. For example, if the temperature is such that collisions preferentially restrict the motion of ions over electrons, it creates a net current. In figure 3.3, collisions tend to stop the ion in the middle of its gyration. As the ion cycloid motion must begin now from the position of the collision, it separates the

ions from the electrons vertically (in this drawing). This is the mechanism for the Pederson current, which flows in the direction of the applied electric field. Similarly, the Hall current is shown in figure 3.3, where collisions preferentially impede the ion from completely its gyration cycle. The inhibited particle must restart from the stopped position much more frequently, causing it to have a slower average velocity than the electron. Therefore, the Hall current is in the -**ExB** direction.

The parallel current, the Pederson current, and the Hall current are all results of an electric field in a conducting medium. They obey Ohm's law and, hence, we refer to them in this paper as Ohmic currents. All other currents are due to drift currents which involve a force, **F**, driving charges across magnetic field lines. As the charge, q , acquires a velocity, it simulates a current moving across the field line. Then, the charge feels a **jxB** force that pushes the charge in the direction perpendicular to both the magnetic field and the original force. Finding the average velocity in the **jxB** direction gives the drift velocity:

$$\mathbf{v}_{drift} = \frac{\mathbf{F} \times \mathbf{B}}{qB^2}$$

Therefore, forces which are independent of charge direct the drift velocities for positive and negative charges opposite directions. In such a situation, the charges separate and there is a net current called the drift current. Because current densities are given by $\mathbf{j}=\Sigma q n_S \mathbf{v}_S$, the total drift current is given by:

$$\mathbf{j}_{drift} = n_i \frac{\mathbf{F}_i \times \mathbf{B}}{B^2} + n_e \frac{\mathbf{F}_e \times \mathbf{B}}{B^2}$$

Resulting from the cross product in the velocity, the drift current is always perpendicular to the magnetic field. Therefore, the drift current never contributes to the field aligned current. Only $j_\perp$ includes drifts.

Some of the drift currents that we include in our modules are the gradient drift, the gravity drift, the drift due to the drag force,

and the curvature drift. The particular forces in the drift currents encountered here are gradients in the magnetic field, $-\mu\nabla B$, gravity, $\rho\mathbf{g}$, the drag force, $\rho\nu\mathbf{v}$, and the curvature of field lines, $mv_{//}^2\mathbf{R}/R^2$. Although the **ExB** drift produces the Hall and Pederson currents through collisions, these currents are not considered drift currents.
Oppositely charged particles **ExB** drift in the same direction leaving no net current. Other drifts naturally produce currents by accelerating unlike charges in opposite directions.

We assume that the drifts, and the Ohmic currents detailed above include all of the significant current sources in the system. These currents should sum to the aggregate current described in section 3.1 needed to completely produce the magnetic field features observed in the solar wind/Venus interaction. There must be direct currents where the magnetic field rotates, while perpendicular currents occur where the magnitude of the field is changing. The model breaks the total current down into their sources and determines the physical mechanisms creating the observed magnetic field structures. This provides a great insight into the physics driving the solar wind interaction with Venus.

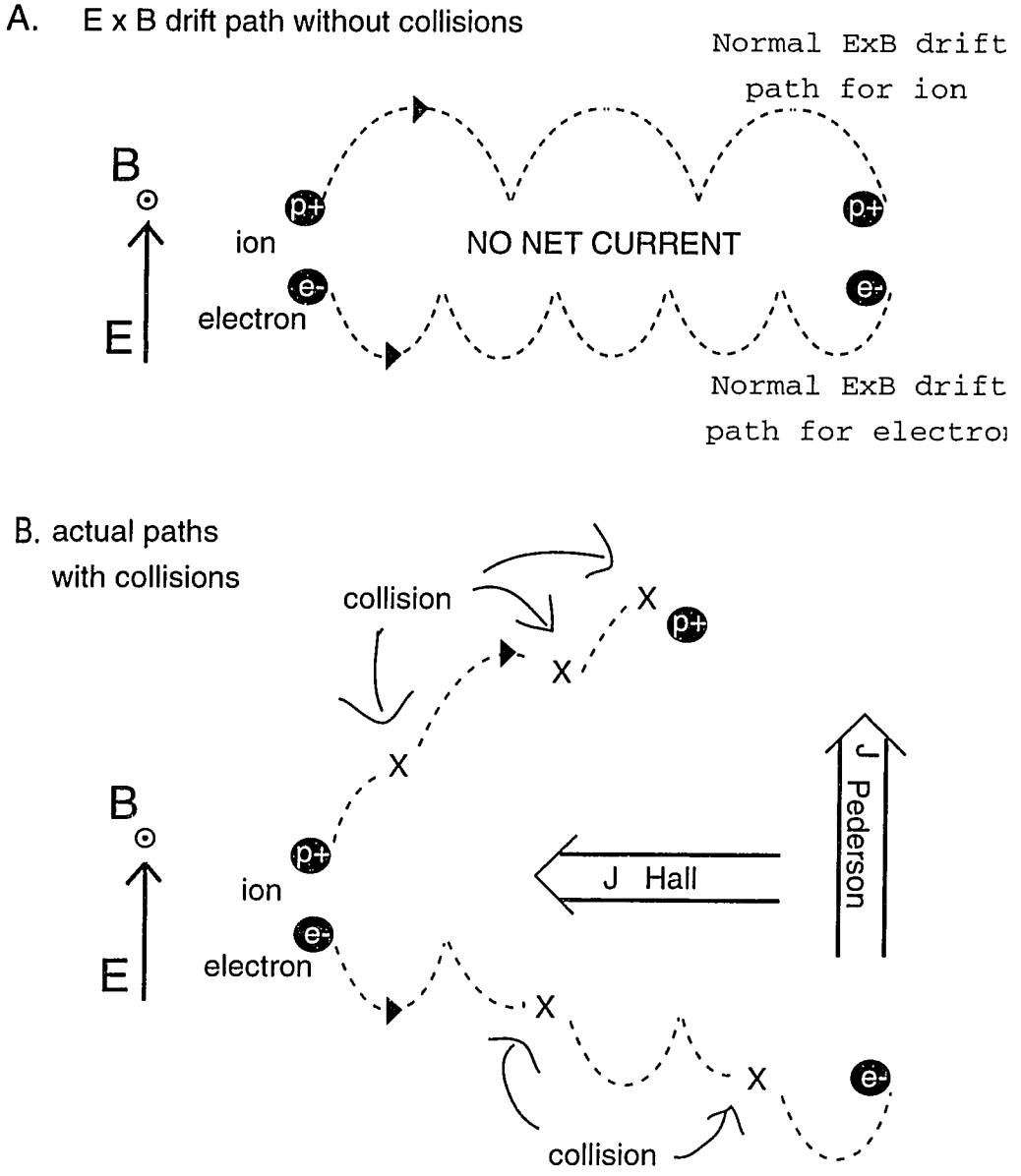

Figure 3.3--Pederson and Hall currents. As electrons and ions E x B drift, they can suffer collisions that cause the particle to change its drift path. If a net current in the direction of the electric field results, it is a Pederson current. If there is a net current in the E x B direction, it is a Hall current. The conductivities of these currents are σ_1 and σ_2 respectively.

4. The Model

This model is both an extension of the Flow/Field model to include the calculation of the electric field and scalar potential as well as an investigation into the physics relevant to the flow of ionospheric currents. We begin with a set of boundary conditions and given parameters. We assume steady state conditions, meaning complete time independence. Next, we analyze the current system to find the mechanisms responsible for driving the interaction. Finally, we calculate the set of unknown parameters in the model. The flow chart in figure 4.1 indicates the order of the program's computations.

First of all, we assume that the magnetic field, **B**, and the current density, **j**, are given either along an orbit trajectory or on a three dimensional grid. We assume that the magnetic field is real, and therefore must satisfy $\nabla \bullet \mathbf{B} = 0$. Also, the current density must be the necessary current for producing the given magnetic field, as described in section 3.1. We rotate **j** at each grid point into a local orthonormal coordinate system that has a basis aligned with the local magnetic field, **B**. The unit vectors of the B-based system are symbolized by **b**, **n**, and **t**. **b** is the unit vector parallel to the magnetic field vector. Therefore, **n** and **t** are perpendicular to **B**. For uniqueness, they are assigned in such a way that **t** has no local vertical component.

Additionally, we assume that several atmospheric parameters are given over the entire calculation grid. For Mars, we have created a model atmosphere based on the Viking 1 & 2 data. Our model incorporates the electron density, ion density, and ion temperature data derived by *Hanson et al* [1977] from Viking's RPA data. The neutral atmosphere is modeled after *Nier and McElroy* [1977]. For Venus, we use atmospheric ion composition and temperatures from representative PVO orbits. The neutral atmosphere is constructed from scale heights and initial values of each constituent. Neither the Mars nor the Venus model atmospheres are highly detailed.

Nonetheless, the atmospheres work appropriately in this diagnostic tool.

The ion density, n_i, is a composite of the density of all the constituent ion species. Likewise, the neutral density, n_n, is the sum of the densities of the dominate neutral species. Treating the individual species, s, the total number density, average mass fraction and mass density are respectively:

$$n_i = \Sigma\, n_s$$
$$\mu_i = \Sigma\, m_s n_s / m_p n_i$$
$$\rho_i = \mu_i m_p n_i$$

where the summations are over all ion species m_s and m_p are the mass of the species and the mass of a proton, respectively. Our models include the three dominate ions in the altitude range of interest--O_2^+, CO^+, and O^+. For both Mars and Venus, the four prevalent neutrals are included and are O, CO_2, N_2 and CO.

Using the model atmosphere, we calculate the collision frequencies at each grid point using the formulas from *Hanson* [*1965*]:

$$\nu_{en} = 5.4 \times 10^{-10} n_n T_e^{1/2}$$
$$\nu_{ei} = [34 + 4.18 \log(T_e^3 / n_e)] n_e T_e^{-3/2}$$
$$\nu_{in} = 2.6 \times 10^{-9} (n_n + n_i) M^{-1/2}$$

where ν is the collision frequency and T_e is the electron temperature. The subscripts e, i and n of ν indicate which two types of particles (of electrons, ions, and neutrals, respectively) are considered in the calculations. When treating the motion of the ions, only collisions with neutrals are considered. The collisions of ions with electrons are not treated because the electrons are so much less massive than the ions that the ions suffer a negligible change in momentum in these interactions. Therefore, only the ion/neutral collisions contribute to the total collision frequency of the ions.

Now we have all the ingredients needed to construct the conductivity tensor. Rotating our vectors into the (t,n,b) coordinate

system simplifies the calculation of the conductivity. In this basis, the tensor components are simply the direct conductivity, σ_0, the Pederson Conductivity, σ_1, and the Hall conductivity, σ_2, in the tensor form:

$$\begin{bmatrix} \sigma_1 & \sigma_2 & 0 \\ -\sigma_2 & \sigma_1 & 0 \\ 0 & 0 & \sigma_0 \end{bmatrix}$$

We proceed by using the conductivity formulas in the Plasma 503 notes [*Wolf*]:

$$\sigma_0 = \frac{n_e e^2}{m_e \nu_{ei} + [\,1/m_e \nu_{en} + Z/m_i \nu_{in}\,]^{-1}}$$

$$\sigma_1 = \frac{n_e e (\zeta + \mu)\lambda}{B[\lambda^2 + (\zeta - \mu)^2]}$$

$$\sigma_2 = \frac{n_e e (\mu^2 - \zeta^2)}{B[\lambda^2 + (\zeta - \mu)^2]}$$

where μ, ζ, and λ are dimensionless quantities defined to simplify the equation as:

$$\mu = \frac{\nu_{en}}{|\omega_{ce}|}$$

$$\zeta = \frac{\nu_{in}}{\omega_{ci}}$$

$$\lambda = \frac{\nu_{ei}}{|\omega_{ce}|}(\mu + \zeta) + 1 + \mu\zeta$$

Here, ω_{ci} and ω_{ce} are the ion and electron cyclotron frequencies. Constructing the conductivity tensor completes the establishment of the planetary atmospheric parameters. We proceed to computing the unknowns.

First of all, we want to calculate the electric field. However, before applying Ohm's Law, we need to analyze our current density. Only part of the total current is due to the electric field. The

remainder is due to drift currents. In general, drift currents take the form:

$$\mathbf{j}_{drift} = n_e \frac{\mathbf{F} \times \mathbf{B}}{B^2}$$

where **F** is any force which accelerates ions and electrons in the same direction, such as those listed in section 3.2. Because of the **FxB** term, drift currents are always perpendicular to the magnetic field. Therefore, the model calculates the total current due to these drifts and subtracts them from the given $j_{\perp}$.

After removing the drift currents, the remainder is all Ohmic current. Then we can directly determine the electric field parallel and perpendicular to the magnetic field using Ohm's Law:

$$\mathbf{j} = \sigma \bullet \mathbf{E}$$

Inverting and defining the Cowling conductivity $\sigma_3 \equiv (\sigma_1^2 + \sigma_2^2)/\sigma_1$, we get the equation:

$$\mathbf{E} = \begin{bmatrix} \frac{1}{\sigma_3} & \frac{-\sigma_2}{\sigma_1^2 + \sigma_2^2} & 0 \\ \frac{\sigma_2}{\sigma_1^2 + \sigma_2^2} & \frac{1}{\sigma_3} & 0 \\ 0 & 0 & \frac{1}{\sigma_0} \end{bmatrix} \bullet \mathbf{j}_{Ohm}$$

which computes the electric field in (t,n,b) coordinates:

The next step is to find the electric potential, V. If the electric field is curl free, then the electric potential can be calculated using Stoke's Theorem, $\Delta V = -\int \mathbf{E} \bullet d\mathbf{s}$. However, if there is a curl, we encounter an inconsistency in the assumptions of the model. By Faraday's Law, the curl in the electric field is due to a time dependent magnetic field. Because we assume time independence, if a time dependence arises, there must be a flaw in the model. Therefore, before we calculate the electric potential, we validate the previous calculations by verifying that the curl of the electric field is zero.

Then, to simplify the calculation of the electric potential on the grid, the electric field is rotated into global (x,y,z) coordinates. In (x,y,z) space, the dot product between the electric field and the path element is easily calculated. The electric field only specifies the potential to an arbitrary constant, so we choose the potential at the sub-flow point to be zero. All potentials are then compared to that. The result is a potential map including all grid points.

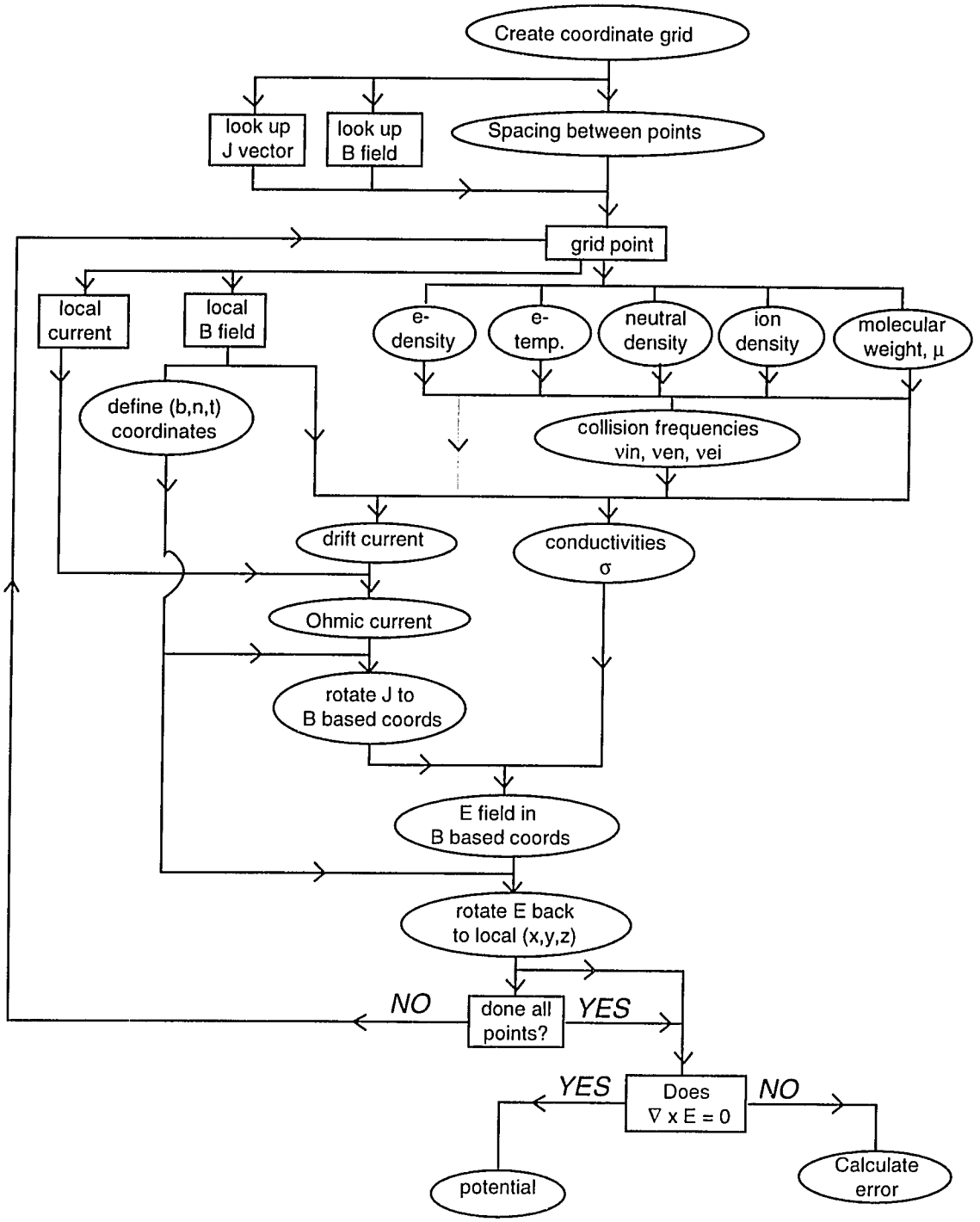

Figure 4.1--Program flow chart.

5. Model Diagnostics

A number of diagnostic tests were performed on the model to evaluate its effectiveness. First of all, each subroutine was individually scrutinized to verify that it does indeed execute its function to within reasonable bounds. After each subroutine was approved, several sample cases were devised which have analytic solutions. The model ran through these cases and compared its output with the analytic results.

5.1 Module Limitations

Each module of the program has its own numerical limitations. Here, we investigate the extent to which the module outputs reliable results by comparing the program's calculations to analytic solutions. Figure 4.1 displays the model's flow chart, in which each individual module is listed.

In the flow chart, the subroutines outlined by a box are routines in which the data is read from a file. These are the given parameters in the problem, which we assume have high accuracy. However, the data is read in as floating point variables. In IDL, floating point variables retain seven significant figures in the mantissa. Therefore, if the input data is known to better than 7 digits, that accuracy is lost at the start of the program. However, the input is usually Pioneer Venus OMAG data, which is generally good to 4 or 5 significant figures. Therefore, we begin the model with an error of 1E-5, at best.

In contrast, the modules in the flow chart that are outlined with ovals contain numerical calculations of some sort. Most of these routines are just algebraic functions of linear quantities. For example, the atmospheric density programs are simple exponentials of the altitude. In most of those modules, the precision is limited by the number of significant figures formulated in the code rather than by round off error. The extreme case is the conductivity program. This routine incorporates all of the atmospheric parameters as well as the magnetic field strength. Consequently,

the worst error for the atmosphere building portion of the model appears in the conductivity. However, analysis indicates that the conductivity tensor computed by the model is very typical of the planetary ionosphere. Therefore, each of the atmospheric programs executes its operation to within acceptable bounds.

Although most modules perform very simple operations, there are some oval modules that differentiate or integrate over a variety of inputs. Namely, these are the drift current program and the potential program. The effectiveness of these routines relies on the form of the given input--generally, a function of the magnetic field--which itself could conceivably be a very high order function of the coordinates. Therefore, we run the modules with highly varying inputs to find the highest order function that the module can handle. These results are described below and listed in figures 5.1 and 5.2.

First of all, the subroutine that calculates the potential, computes the path integral of the electric field vector. Evaluation of the program shows that it is effective for integrating a function of any one spatial variable of order $< O(x_i^3)$. In the case when several spatial variables are present, the program works to better than 1% for order $< O(x^5)$. Of course, the precision for calculating trigonometric functions depends on the relative size of the spacing between grid points and the wavelength of the trigonometric function. Therefore, those results are not shown here. However, figure 5.1 lists the results for some specific trial functions.

resulting	ave. err.	std. dev.	max. err	% > 5%	% > 1%
√x	0.03	0.04	0.15	10	50
xyz	1E-7	1E-7	5E-7	0	0
(xyz)^2	1E-5	7E-5	1E-3	0	0
(xyz)^3	2E-3	1E-2	0.15	0.8	3
x^4	1E-7	2E-7	4E-7	0	0
x^5	0.32	0.94	3.2	10	30

Figure 5.1--The error for the different inputs into the integration routine. The first column is the function resulting from integration. The second and third columns are the error and standard deviation. Column 4 is the maximum error for all the grid points. Columns 5 and 6 denote the percentage of grid points with error exceeding the given value.

input	direction	ave. err.	st. dev.	max. err
x^2	x	4E-8	5E-8	2E-7
xy^2	y	1E-7	2E-7	8E-7
z^4	z	4E-5	4E-5	9E-5

Figure 5.2--The error for the different inputs into the differentiation routine. The first column is the differentiated function. The second column denotes the direction of the derivative. The third and fourth columns are the error and standard deviation. Column 5 is the maximum error for all the grid points.

Second, there are many instances in which the model calculates a derivative. For example, we take the curl of the electric field to verify that the field is curl free (ensuring time independence). Also, if the current is not given, it is calculated by the curl of the magnetic field. In addition, the gradient drift includes the calculation of the gradient of the magnetic field. The general differentiation routine fits a quadratic function to the closest three grid points in the direction of differentiation. Then, the derivative at the midpoint is simply the value of the derivative of the quadratic evaluated at that point. This guarantees precision to IDL's round off limit of 10^{-7} for functions of order $< O(x^2)$. Testing shows that the routine does not fall to error worse than 1% until functions of order $> O(x^4)$ for fine grid spacing. As with the integration routine, its effectiveness is highly dependent on the coarseness of the grid. The results from the evaluations appear in figure 5.2.

Now that we are confident that the modules perform to within expectations on an individual basis, we proceed to test several sample cases on the entire model. This ensures that the model functions correctly as a whole. Each of the trials below probes a different aspect of the model.

5.2 Trial Cases

Trial Case 1--all perpendicular current, no drift

Consider the case in which the ionosphere is a rectangular box with a constant conductivity tensor. If magnetic field and current geometry are simple enough, the electric field and potential can be

found analytically. For the first trial case, we investigate the situation in which there are only perpendicular currents. Assume the electric potential is of the form:

$$V = -yz$$

where y and z are simply the spatial coordinates (y is horizontal and z is vertical). Assuming time independence, the electric field can be calculated by:

$$\mathbf{E} = -\nabla V = y\mathbf{z} + z\mathbf{y}$$

The electric field in a conducting ionosphere drives a current given by Ohm's Law:

$$\mathbf{j}_{ohm} = \begin{bmatrix} \sigma_1 & \sigma_2 & 0 \\ -\sigma_2 & \sigma_1 & 0 \\ 0 & 0 & \sigma_0 \end{bmatrix} \bullet \mathbf{E}$$

In order to use this, the vectors **j** and **E** must be in a coordinate system with one basis aligned with the local magnetic field, such as the (t,n,b) system described in chapter 4. Therefore, we must define the direction of the magnetic field. We select it to be in the **x** direction. Then, the basis states relate to the (x,y,z) system by the following matrix:

$$\begin{bmatrix} \mathbf{t} \\ \mathbf{n} \\ \mathbf{b} \end{bmatrix} = \begin{bmatrix} 0 & 1 & 0 \\ 0 & 0 & 1 \\ 1 & 0 & 0 \end{bmatrix} \begin{bmatrix} \mathbf{x} \\ \mathbf{y} \\ \mathbf{z} \end{bmatrix} = \begin{bmatrix} \mathbf{y} \\ \mathbf{z} \\ \mathbf{x} \end{bmatrix}$$

Rotating the electric field and the current into the (t,n,b) coordinate system and applying Ohm's law, we get:

$$\mathbf{j}_{Ohm} = \sigma \bullet \mathbf{E}_{B\text{-based}} = \begin{bmatrix} \sigma_1 & \sigma_2 & 0 \\ -\sigma_2 & \sigma_1 & 0 \\ 0 & 0 & \sigma_0 \end{bmatrix} \begin{bmatrix} z \\ y \\ 0 \end{bmatrix}$$

$$= (\sigma_1 z + \sigma_2 y)\mathbf{y} + (\sigma_1 y - \sigma_2 z)\mathbf{z}$$

This is only the current due to the electric fields. The total current, the current needed to produce the overall magnetic field, is the sum

of the current calculated above and the drift current. Knowing that the Ohmic current, in this case, is totally perpendicular to the magnetic field and that the drift current is always a perpendicular current, we have no parallel current in this problem. Therefore, the total current is in the **y** and **z** directions. The simplest magnetic field that results from such a current is a function of y and z in the **x** direction:

$$\mathbf{B} = f(y,z)\mathbf{x}$$

Using Gauss's Law to find the total current:

$$\mathbf{j} = \frac{\nabla \times \mathbf{B}}{\mu_o} = \frac{1}{\mu_o}\left(\frac{\delta f}{\delta z}\mathbf{y} - \frac{\delta f}{\delta y}\mathbf{z}\right) = \mathbf{j}_{ohm} + \mathbf{j}_{drift}$$

$$= (\sigma_1 z + \sigma_2 y + \mathbf{j}_{y\text{-}drift})\mathbf{y} + (\sigma_1 y - \sigma_2 z + \mathbf{j}_{z\text{-}drift})\mathbf{z}$$

Due to the unphysical nature of the example problem, we can arbitrarily define the drift current to suit the calculation. In this case, the current from Ohm's law satisfies Gauss's law on its own. The addition of a drift current only alters the magnetic field magnitude here. Therefore, we set the drift current equal to zero. This determines the magnetic field is to be:

$$\mathbf{B} = \mu_o\left(\frac{\sigma_1 z^2}{2} + \sigma_2 yz - \frac{\sigma_1 y^2}{2}\right)$$

So, using the above **B**, **j**, and $\mathbf{j}_{drift}$ as inputs to the model, we calculate the electric field and potential and compare those values with the expected values. The electric fields agree to better than 10^{-7}. The potential is calculated correctly to 10^{-6}.

Trial Case 2--all perpendicular current, with drift

As a second test, we use a potential similar to the one above, except it requires the addition of a drift current. We start with:

$$V = -yz^2$$

$$\mathbf{E} = -\nabla V = z^2\mathbf{y} + 2yz\mathbf{z}$$

$$\mathbf{B} = f(y,z)\mathbf{x}$$

$$\mathbf{j}_{ohm} = (\sigma_1 z^2 + 2\sigma_2 yz)\mathbf{y} + (2\sigma_1 yz - \sigma_2 z^2)\mathbf{z}$$

$$\mathbf{j} = \mathbf{j}_{Ohm} + \mathbf{j}_{drift} = \frac{1}{\mu_o}\left(\frac{\delta f}{\delta z}\mathbf{y} - \frac{\delta f}{\delta y}\mathbf{z}\right)$$

We choose a magnetic field that comes close to satisfying Gauss's Law by integrating the Ohmic current:

$$B_{x,y-Ohm} = \mu_o \int j_{y-Ohm}\, dz = \mu_o \frac{\sigma_1 z^3}{3} + \mu_o \sigma_2 yz^2$$

$$B_{x,z-Ohm} = \mu_o \int j_{z-Ohm}\, dy = \mu_o \sigma_2 yz^2 - \frac{\mu_o \sigma_1 y^2 z}{3}$$

$$B_x = \mu_o\left(\frac{\sigma_1 z^3}{3} + \sigma_2 yz^2 - \frac{\sigma_1 y^2 z}{3}\right)$$

Taking the curl of this magnetic field gives us the Ohmic current above with some surplus. The surplus is the drift current and it is equal to $-2\sigma_1 y^2\,\mathbf{y}$.

In the execution of this regime, we find a nuance in the numerics of the model. If the magnetic field magnitude drops to zero (or very close to zero), there is difficulty in determining the direction of the magnetic field. Therefore, problems arise in aligning the other vectors with the very uncertain (t,n,b) coordinate system. Moreover, calculation of the inverse rotation matrix can involve division by extremely small numbers that promotes one direction to an enormous magnitude. This poses a significant problem for analysis of real data because many PVO orbits show a largely unmagnetized lower ionosphere. Figure 5.3 displays the magnetic field magnitude profiles for 3 consecutive PVO inbound orbits--175, 176, and 177. Orbit 175 exhibits a rapidly fluctuating, low intensity magnetic field. This is dubbed a "drop-out" field and is probably associated with the presence of flux ropes in the lower ionosphere. In contrast, orbit 176 depicts a strong and steady field profile. Further, the magnetic field for orbit 177 behaves

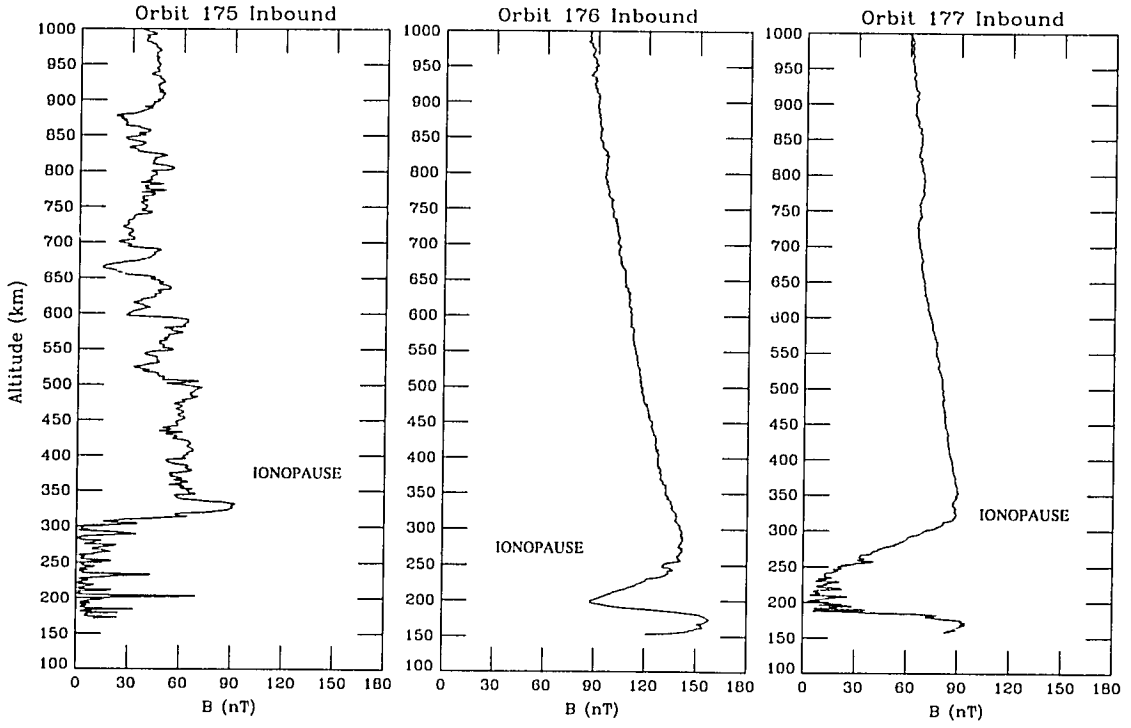

Figure 5.3--The magnetic field magnitude profile for PVO orbits 175, 176, and 177. These profiles are very different even though they are from sequential PVO orbits. Orbit 175 is an instance of "drop-out" magnetic field, which occurs under high solar wind pressure. In contrast, the magnetic field during orbit 176 is very strong and smooth. And, the conditions for orbit 177 lie somewhere in between. *(Courtesy of C. Law)*

differently in that it never drops to zero, but does fluctuate strongly. In addition, as the plot of the field direction in figure 1.1 indicates, the angle of the field can rotate wildly at low altitudes. Therefore, before the model is run on real data, we must insert a module that treats "drop-out magnetic field" cases.

For the test case, we avoid the problem by adding a constant to the magnetic field equal to twice its minimum value. The constant drops out of all other parameters in the subsequent calculations. With this, the model reproduces the analytic results quite nicely. No error for any calculated parameter at any grid point is greater than 4E-5. Satisfied that the model can treat any reasonable perpendicular current, we analyze the workings with parallel current.

Trial Case 3--all parallel current

Now, consider the case with only parallel currents. To get such a current, we use a magnetic field and total current of the form:

$$\mathbf{B} = B_o \left(\cos\left(\pi z / 2 z_{max}\right)\mathbf{x} + \sin\left(\pi z / 2 z_{max}\right)\mathbf{y}\right)$$

$$\mathbf{j} = \frac{-B_o}{\mu_o}\left(\cos\left(\pi z / 2 z_{max}\right)\mathbf{x} + \sin\left(\pi z / 2 z_{max}\right)\mathbf{y}\right)$$

We know that the Ohmic current is the only current that can comprise the parallel current. Therefore, the electric field parallel to the magnetic field is exactly determined by:

$$E_b = j/\sigma_0$$

However, because the curl of E_b does not equal zero on its own, there must be a perpendicular electric field present to avert a possible time dependence. To simplify the calculation, we let E_t equal zero and let E_n (= E_z) cancel the curl in E_b. Solving, we find the electric field and the potential to be:

$$\mathbf{E} = \frac{-B_o \pi}{2\mu_o \sigma_0 z_{max}}\left(\begin{array}{l}\cos\left(\frac{\pi z}{2 z_{max}}\right)\mathbf{x} + \sin\left(\frac{\pi z}{2 z_{max}}\right)\mathbf{y} \\ + \frac{\pi}{2 z_{max}}\left(y\cos\left(\frac{\pi z}{2 z_{max}}\right) - x\sin\left(\frac{\pi z}{2 z_{max}}\right)\right)\mathbf{z}\end{array}\right)$$

$$V = \frac{B_o \pi}{2\mu_o \sigma_0 z_{max}}\left(x\cos\left(\frac{\pi z}{2 z_{max}}\right) + y\sin\left(\frac{\pi z}{2 z_{max}}\right)\right)$$

The presence of E_n leads to an Ohmic current perpendicular to the magnetic field. In order to keep the current completely parallel, we must have a drift current cancel the perpendicular Ohmic current. This drift current is equal to $-\sigma_2 E_n \mathbf{t} - \sigma_1 E_n \mathbf{n}$.

Running this model, the output matches the analytic results fairly well. The electric field in the **z** direction has .4% of the grid points with errors greater than 1%. However, the worst error in the potential calculation is 1E-3 with an average error of 1E-4.

Therefore, we conclude that the model is capable of processing parallel currents.

Trial Case 4--spherical shell atmosphere, perpendicular current

For this trial case, we investigate how the modules work in spherical coordinates. There are only a few differences when the program runs on a spherical grid from when it runs on a Cartesian grid. First of all, the derivatives involve extra factors. Therefore, if the coordinate flag indicates a spherical grid, it inserts the necessary factors for differentiation in programs such as the drift program and the routine that verifies that $\nabla \times \mathbf{E} = 0$. Also, because the grid is in spherical coordinates, we must be careful in specifying the path element vector to the Stoke's theorem module. In spherical coordinates, $d\mathbf{s}$ is $d\mathbf{r} = dr\ \mathbf{r} + r\, d\theta\ \boldsymbol{\theta} + r \sin(\theta)\, d\phi\ \boldsymbol{\phi}$. Otherwise, the program handles a spherical grid in the same way as it does a rectangular grid.

We set up a grid with equal spacing in r, θ and ϕ, where r is the distance to the center of the planet, θ is the angle with the z axis and ϕ is the azimuthal angle. The global (x,y,z) coordinates corresponding to this system are centered on the center of the planet with the x axis pointing towards the Sun, the y axis is in the direction of orbital velocity, and the z axis is perpendicular to the plane of motion.

Then, we establish a magnetic field in the ϕ direction that results in a current in the θ direction only:

$$\mathbf{B} = \frac{B_o}{\sin\theta}\boldsymbol{\phi}$$

$$\mathbf{j} = \frac{-B_o}{\mu_o r \sin\theta}\mathbf{r}$$

thus making our (t,n,b) unit vectors (θ,-r,ϕ). Because there is no parallel current, the electric field only has perpendicular components. In general, we expect the electric field to be a function of r and θ in both perpendicular directions:

$$\mathbf{E} = f(r, \theta)\,\boldsymbol{\theta} + g(r, \theta)\,\mathbf{r}$$

In order for the electric field to be curl-free, we require :

$$\frac{\partial (rf(r,\theta))}{\partial r} = \frac{\partial g(r,\theta)}{\partial \theta}$$

In order to have an electric field of this form produce an Ohmic current close to the total current, we set the electric field equal to:

$$\mathbf{E} = -\sigma_1/\sigma_2 r\ \theta + 1/r\ \mathbf{r}$$

The corresponding Ohmic current is:

$$\mathbf{j}_{Ohm} = -(\sigma_1^2+\sigma_2^2)/\sigma_2 r\ \theta$$

and the electric potential:

$$V = \frac{\sigma_1}{\sigma_2}\left(\theta - \frac{\pi}{2}\right) - \ln\ \left(\frac{r}{r_o}\right)$$

The results of this trial case are very good. The worst error at any grid point for the electric field or the electric potential was 5E-5. Therefore, the special modules for handling spherical coordinates perform satisfactorily.

Each of the four trial cases above tests different components of the model. Together, they demonstrate that the model outputs parallel and perpendicular electric fields to within 1% of the correct value. The model also creates a reliable potential map. Furthermore, the model works in either a spherical or rectangular geometry. From the analysis above, we believe that the model is ready to process real data. Therefore, we look forward to the upcoming uses for the model developed and tested here.

6. Conclusion

The validity of this model is proven with the success of the simple test scenarios. Now that the model is constructed, we plan to follow several avenues to progress the understanding of the interaction of the solar wind with Mars. Most simply, we apply the Flow/Field model to the specific environments of Venus and Mars, and make direct comparisons between their interactions with the solar wind. With the benefit of the additional laboratory of Mars to test theories, we gain more insight on the physics involved. Specifically, we can examine the effects that the size of the planet and the density of the ionosphere and atmosphere have on the interaction. Because the atmosphere of Mars is less substantial than that at Venus, we expect Mars to behave much like Venus under high solar wind pressure. Therefore, the application of the Flow/Field model to Mars permits a means for determining relationships between parameters without being specific to one planet.

Second, we incorporate a global current system into the Flow/Field model. This current system has been discovered by *Law and Cloutier* [1995] and is the electric current density needed to produce the global magnetic field. By breaking the overall current into physically meaningful components, such as drift currents, direct current, and Pederson and Hall currents, we learn under which processes the currents are driven through the ionosphere. This provides a great insight into the driving mechanisms of the interaction.

Additionally, we supplement the dayside model with some recent work on the nightside current system [*Walker* pers. com.]. Using the new three dimensional model and the nightside picture, we can investigate changes in parameters over solar zenith angle. With the nightside picture, we can also study the flow across the terminator. To date, this flow is quite perplexing.

Once we understand the interaction of the solar wind with Venus, we can test our understanding on Mars. We prepare for the

MGS mission by calculating with the model what we expect the magnetometer aboard the Mars Global Surveyor to measure along its trajectory, once it is inserted into Mars orbit. Once data returns, it will immediately answer the questions, "Does Mars have an intrinsic magnetic field?" and "Do we understand the physics of the interaction?". When we compare the magnetic field verses time data from the spacecraft with the model's results, we will discover whether or not they match. If the model accurately represents the *in situ* data, we can conclude that our model accurately represents the physics of the interaction and that the magnetic field of Mars is negligible. We can then place a firm upper limit to the weak magnetic field of Mars.

Furthermore, the model produces a map of the global electric potential. Given an atmosphere and a magnetic field configuration, the model calculates the global current density, the conductivity tensor, then the electric field, and finally the potential. Knowing the potential helps to check the overall energy budget of interaction. In the same vain, we can use the potential map capabilities to maximize the knowledge obtained from Mars Global Surveyor. Its magnetometer will measure the magnetic field. Meanwhile, the model will take that data and find the current, electric field, and potential.

In summary, there are several interesting subjects to investigate using the model that is developed here. Many of these topics follow directly from this work, although others require further modifications to the model. Naturally, the MGS portion relies on the timely success of the spacecraft. Therefore, barring any misfortune, I will pursue these roads in my future research.

References

Bogdanov, AV and OL Vaisberg. Structure and Variations of Solar Wind-Mars Interaction Region, *Journal of Geophysical Research*, 80, 4, 487-494, 1975.

Brecht, SH and JR Ferrante. Global Hybrid Simulation of Unmagntized Planets: Comparison of Venus and Mars, *Journal of Geophysical Research*, 96, A7, 11209-11220, 1991.

Breus, TK, AM Krymskii, R Lundin, EM Dubinin, JG Luhmann, Ye Yeroshenko, SV Barabash, VYa Mitnitskii, NF Pissarenko, and VA Styashkin. The Solar Wind Interaction with Mars: Consideration of Phobos 2 Mission Observations of an Ion Composition Boundary on the Dayside, *Journal of Geophysical Research*, 96, A7, 11165-11174, 1991.

Cloutier, PA, MB McElroy and FC Michel. Modification of the Martian Ionosphere by the Solar Wind, *Journal of Geophysical Research*, 74, 26, 6215-6228, 1969.

Cloutier, PA and RE Daniell. Ionospheric Currents Induced by Solar Wind Interaction with Planetary Atmospheres, *Planetary and Space Science*, 21, 463-474, 1973.

Cloutier, PA, RE Daniell, and DM Butler. Atmospheric Ion Wakes of Venus and Mars in the Solar Wind, *Planetary and Space Science*, 22, 967, 1974.

Cloutier, PA and RE Daniell. An Electrodynamic Model of the Solar Wind Interaction with the Ionospheres of Mars and Venus, *Planetary and Space Science*, 27, 1111-1121, 1979.

Cloutier, PA, TF Tascione, RE Daniell, HA Taylor, and RS Wolf. Physics of the Interaction of the Solar Wind with the Ionosphere of Venus: Flow/Field Models, in *Venus*, edited by DM Hunten, L Colin, TM Donahue, and VI Moroz, 941-979, U. Arizona Press, Tucson, 1983.

Cloutier, PA, HA Taylor and JE McGary. Steady State Flow/Field Model of Solar Wind Interaction with Venus: Global

Implications of Local Effects, *Journal of Geophysical Research*, 92, A7, 7289-7307, 1987.

Dolginov, Sh Sh. On the Magnetic Field of Mars: Mars 2 and 3 Evidence, *Geophysical Research Letters*, 5, 1, 89-93, 1978.

Dubinin, E, R Lundin, W Riedler, K Schwingenschuh, JG Luhmann, CT Russell, and LH Brace. Comparison of Observed Plasma and Magnetic Field Structures in the Wakes of Mars and Venus, *Journal of Geophysical Research*, 96, A7, 11,189-11197, 1991.

Foukal, PV. *Solar Astrophysics*, John Wiley & Sons,Inc., New York: 1990.

Hanson, WB. "Structure of the Ionosphere" in *Satellite Environment Handbook*, edited by FS Johnson, Stanford University Press, Stanford: 1965.

Hanson, WB, S Sanatani, and DR Zuccaro. The Martian Ionosphere as Observed by the Viking Retarding Potential Analyzers, *Journal of Geophysical Research*, 82, 4351-4363, 1977.

Hantsch, MH and SJ Bauer. Solar Control of the Mars Ionosphere, *Planetary and Space Science*, 38, 4, 539-542, 1990.

Intriligator, DS and EJ Smith. Mars in the Solar Wind, *Journal of Geophysical Research*, 84, B14, 8427-8435, 1979.

Kramer, L, PA Cloutier and HA Taylor. Model of Superthermal Ions in the Venus Ionosphere, *Journal of Geophysical Research*, 98, A3, 3645-3658, 1993.

Law, CC. Observations of Magnetic Signatures and structure in the dayside ionosphere of Venus, M. S. Thesis, Department of Space Physics & Astronomy, Rice University, 1994.

Law, CC. Currents and Magnetic Field Structures in the Dayside Solar Wind Interaction with Venus and Mars, Ph.D. Thesis, Department of Space Physics & Astronomy, Rice University, 1995.

Law, CC and PA Cloutier. Observations of Magnetic Structure at the Dayside Ionopause of Venus, *Journal of Geophysical Research*, 100, A12, 23,973-23,981, 1995.

Luhmann, JG, CT Russell, FL Scarf, LH Brace and WC Knudsen. Characteristics of the Marslike Limit of the Venus-Solar Wind Interaction, *Journal of Geophysical Research*, 92, A8, 8545-8557, 1987.

Luhmann, JG and K Schwingenschuh. A Model of the Energetic Ion Environment of Mars, *Journal of Geophysical Research*, 95, A2, 939-945, 1990.

Luhmann, JG, CT Russell, K Schwingenschuh, and Ye Yeroshenko. A Comparison of Induced Magnetotails of Planetary Bodies: Venus, Mars, and Titan, *Journal of Geophysical Research*, 96, A7, 11199-11208, 1991.

Lundin, R, A Zakharov, R Pellinen, H Borg, B Hultqvist, N Pissarenko, EM Dubinin, SW Barabash, I Liede, and HK Oskinen. First Measurements of the Ionospheric Plasma Escape from Mars, *Nature*, 341, 609-612, 1989.

Mahajan, KK and HG Mayr. Mars Ionopause during Solar Minimum: A Lesson from Venus, *Journal of Geophysical Research*, 95, A6, 8265-82690, 1990.

Nagy, AF, TI Gombosi, K Szego, RZ Sagdeev, VD Shapiro, and VI Shevchenko. Venus Mantle-Mars Planetosphere: What are the Similarities and Differences?, *Geophysical Research Letters*, 17, 6, 865-868, 1990.

Riedler, W, D Mohlmann, VN Oraevsky, K Schwingenschuh, Ye Yeroshenko, J Rutenback, Oe Aydogar, G Berghofer, H Lichtenegger, M Delva, G Schelch, K Pirsch, G Fremuth, M Steller, H Arnold, T Radisch, U Auster, KH Fornacon, HJ Schenk, H Michaelis, U Motschmann, T Roatsch, K Sauer, R Schroter, J Kurths, D Lenners, J Linthe, V Kobezev, V Styashkin, J achache, J Slavin, JG Luhmann, and CT Russell. Magnetic Field near Mars, *Nature*, 19, 341, 604-607, 1989.

Russell, CT, JG Luhmann, JR Spreiter, and SS Stahara. The Magnetic Field of Mars: Implications from Gas Dynamic Modeling, *Journal of Geophysical Research*, 89, 2997-3003, 1984.

Sagdeev, RZ, VD Shapiro, VI Shevchenko, A Zacharov, P Király, K Szegó, AF Nagy, and RJL Grard. Wave Activity in the Neighborhood of the Bowshock of Mars, *Geophyical Research Letters*, 17, 6, 893-896, 1990.

Sauer, K, A Bogdanov, and K Baumgärtel. Evidence of an Ion Composition Boundary in Bi-ion Fluid Simulations of Solar Wind Mass Loading, *Geophysical Research Letters*, 21, 20, 2255-2258, 1994.

Sauer, K, T Roatsch, K Baumgärtel, and JF McKenzie. Transition to Supersonic Flow in Planetary Ionospheres.

Sauer, K, T Roatsch, U Motschmann, K Schwingenschuh, R Lundin, H Rosenbauer, and S Livi. Observations of Plasma Boundaries and Phenomena around Mars with Phobos 2, *Journal of Geophysical Research*, 97, A5, 6227-6233, 1992.

Shinagawa, H and TE Cravens. A One Dimensional Multispecies Magnetohydrodynamic Model of the Dayside Ionosphere of Mars, *Journal of Geophysical Research*, 94, A6, 6506-6516, 1989.

Shinigawa, H , J Kim, AF Nagy, and TE Cravens. A Comprehensive Magnetohydrodynamic Model of the Venus Ionosphere, *Journal of Geophysical Research*, 96, A7, 11,083-11095, 1991.

Slavin, JA, K Schwingenschuh, W Riedler, and Ye Yeroshenko. The Solar Wind Interaction with Mars: Mariner 4, Mars 2, Mars 3, Mars 5, and Phobos 2 Observations of Bow Shock Position and Shape, *Journal of Geophysical Research*, 96, A7, 11235-11241, 1991.

Spreiter, JR and SS Stahara. A New Predictive Model for Determining Solar Wind-Terrestrial Planet Interactions, *Journal of Geophysical Research*, 85, 6769-6777, 1980.

Spreiter, JR, AL Summers, and AW Rizzi. Solar Wind Flow Past Nonmagnetic Planets--Venus and Mars, *Planetary and Space Science*, 18, 1281-1298, 1970.

Stewart, BK. A Modified Flow/Field Model of the Solar Wind Interaction with Mars, PhD thesis, Department of Space Physics and Astronomy, Rice University, 1991.

Tanaka, T. Configurations of the Solar Wind Flow and Magnetic Field around the Planets with no Magnetic Field: Calculation by a New MHD Simulation Scheme, *Journal of Geophysical Research*, 98, A10, 17251-17262, 1993.

Walker, PW. M.S. Thesis, Department of Space Physics and Astronomy, Rice University, in progress.

Wang, Y-M, AG Nash and NR Sheeley Jr. Magnetic Flux Transport on the Sun, *Science*, 245, 681-796, 1989.

Wang, Y-M, SH Hawley and NR Sheeley Jr. The Magnetic Nature of Coronal Holes, *Science*, 271, 464-469, 1996.

Zhang, TL, K Schwingenschuh, H Lichtenegger, W Riedler, CT Russell, and JG Luhmann. Interplanetary Magnetic Field Control of the Mars Bow Shock: Evidence for a Venuslike Interaction, *Journal of Geophysical Research*, 96, A7, 11265-11269, 1991.